

The transmission spectrum of WASP-17 b from the optical to the near-infrared wavelengths: combining STIS, WFC3 and IRAC datasets

ARIANNA SABA,¹ ANGELOS TSIARAS,^{2,1} MARIO MORVAN,¹ ALEXANDRA THOMPSON,¹ QUENTIN CHANGEAT,¹
 BILLY EDWARDS,^{3,1} ANDREW JOLLY,^{4,1} INGO WALDMANN,¹ AND GIOVANNA TINETTI¹

¹Department of Physics and Astronomy, University College London, Gower Street, WC1E 6BT London, United Kingdom

²INAF - Osservatorio Astrofisico di Arcetri, Largo E. Fermi 5, 50125 Firenze, Italy

³AIM, CEA, CNRS, Université Paris-Saclay, Université de Paris, F-91191 Gif-sur-Yvette, France

⁴School of Physics, University of New South Wales, Sydney, NSW 2052, Australia

ABSTRACT

We present the transmission spectrum of the inflated hot-Jupiter WASP-17 b, observed with the STIS and WFC3 instruments aboard the Hubble Space Telescope, allowing for a continuous wavelength coverage from ~ 0.4 to ~ 1.7 μ m. Observations taken with IRAC channel 1 and 2 on the Spitzer Space Telescope are also included, adding photometric measurements at 3.6 and 4.5 μ m. HST spectral data was analysed with Iraclis, a pipeline specialised in the reduction of STIS and WFC3 transit and eclipse observations. Spitzer photometric observations were reduced with the TLCD-LSTM method, utilising recurrent neural networks. The outcome of our reduction produces incompatible results between STIS visit 1 and visit 2, which leads us to consider two scenarios for G430L. Additionally, by modelling the WFC3 data alone, we can extract atmospheric information without having to deal with the contrasting STIS datasets. We run separate retrievals on the three spectral scenarios with the aid of TauREx 3, a fully Bayesian retrieval framework. We find that, independently of the data considered, the exoplanet atmosphere displays strong water signatures and potentially, the presence of aluminium oxide (AlO) and titanium hydride (TiH). A retrieval that includes an extreme photospheric activity of the host star is the preferred model, but we recognise that such a scenario is unlikely for an F6-type star. Due to the incompleteness of all STIS spectral lightcurves, only further observations with this instrument would allow us to properly constrain the atmospheric limb of WASP-17 b, before JWST or Ariel will come online.

1. INTRODUCTION

In recent years, the *Hubble Space Telescope* has been at the forefront of exoplanet atmospheric characterisation. Thanks to its Wide Field Camera 3 (WFC3) and its Space Telescope Imaging Spectrograph (STIS), often combined with the InfraRed Array Camera (IRAC) aboard the *Spitzer Space Telescope*, the atmosphere of hot-Jupiters (Sing et al. 2016; Tsiaras et al. 2018; Pinhas et al. 2018; Skaf et al. 2020; Pluriel et al. 2020b), ultra-hot-Jupiters (Kreidberg et al. 2018; Mikal-Evans et al. 2019; Edwards et al. 2020a; Changeat et al. 2020), super-Earths (Tsiaras et al. 2016b, 2019; Edwards et al. 2020b; Mugnai et al. 2021), sub-Neptunes (Guo et al. 2020; Guilluy et al. 2020) and hot-Saturns (Anisman et al. 2020; Carone et al. 2021) have been studied in transmission, emission and across their phase-curves (Knutson et al. 2012; Stevenson et al. 2017; Kreidberg et al. 2018; Arcangeli et al. 2019; Irwin et al. 2020; Feng et al. 2020; Changeat et al. 2021). Although small rocky plan-

ets are difficult to probe with current spectrographs due to the limited signal to noise ratio of their gaseous envelope, atmospheric studies conducted on extrasolar gas giants reported the detection of various molecules, in particular water vapour.

Among the exoplanet population of inflated hot-Jupiters, WASP-17 b (Anderson et al. 2010) is one of the least dense planets discovered so far, with a radius equal to 1.932 ± 0.053 R_J and a mass 0.477 times that of Jupiter (Southworth et al. 2012). The transiting planet, confirmed to possess a retrograde orbit (Bayliss et al. 2010; Hébrard et al. 2011; Simpson et al. 2011), forms an angle of $148.5^\circ \pm 5.1^\circ$ with respect to the rotation axis of its parent star (Triaud et al. 2010). The considerable orbital obliquity of WASP-17 b cannot be explained by inward migration (Lin et al. 1996; Ida & Lin 2004) but could be rather due to an initial misalignment between the star and the protoplanetary disk (Bate et al. 2010), planet-planet scattering or the Kozai mechanism (Nagasawa et al. 2008). These processes also induce the

very small eccentricities reported in orbitally misaligned planets (Bourrier et al. 2018; Johnson et al. 2009; Winn et al. 2009): in fact, Southworth et al. (2012) were not able to find any evidence of the orbital eccentricity of WASP-17b. The exoplanet takes 3.7 days to orbit its host star (Southworth et al. 2012), a F6-type star with $V_{mag}=11.6$ (Anderson et al. 2010).

Given the planet's very large atmospheric scale height (Anderson et al. 2010), transmission spectroscopy studies have been extremely successful. From the ground, sodium was detected at optical wavelengths by Wood et al. (2011) and Zhou & Bayliss (2012) using the VLT, and with the Magellan Telescope by Khalfinejad et al. (2018). At low-resolution, the spectrograph FORS2 mounted on the VLT detected potassium in the atmosphere of WASP-17b with a 3σ significance and water absorption (Sedaghati et al. 2016). From space, data taken with HST in the optical and near-infrared and with Spitzer at $3.6\ \mu\text{m}$ and $4.5\ \mu\text{m}$, report water absorption and alkali features, with little to no clouds/hazes (Sing et al. 2016). A more recent atmospheric study on WASP-17b (Alderson et al. 2022) further confirms the presence of H_2O in addition to CO_2 absorption in the infrared. Lastly, the study conducted by Barstow et al. (2016) reports the presence of water at solar abundances in the limb of WASP-17b, possibly accompanied by CO signatures. However, contrary to the results by Sing et al. (2016), their best atmospheric model includes scattering aerosols at relatively high altitudes, up to 1 mbar.

Here we present the spectroscopic analysis performed on transit observations taken with STIS (gratings G430L and G750L) and WFC3 (grisms G102 and G141) onboard the *Hubble Space Telescope* and with IRAC channel 1 and 2 of the *Spitzer Space Telescope*. The combination of the aforementioned instruments allows us to investigate the spectrum of WASP-17b from the optical to the near infrared wavelengths (0.4 - 5 μm).

2. METHODOLOGY

2.1. *HST* data processing

2.1.1. WFC3

We downloaded the HST/WFC3 raw spectroscopic and spatially scanned observations of WASP-17b from the Mikulski Archive for Space Telescopes (MAST), as part of the HST Proposal 14918 (P.I. Hannah Wakeford). In our study we decided to not include the HST/WFC3 dataset from proposal 12181, obtained in staring mode, because of its low S/N. The data would produce error bars 6 to 7 times bigger compared to the other WFC3 observations, obtained in spatial scanning mode.

Table 1. Stellar and planetary parameters for WASP-17b used for the data reduction with Iraclis and TLCD-LSTM, and the atmospheric modelling with TauREx 3.

Stellar & Planetary Parameters	
T_* [K]	6550 ± 80 *
R_* [R_\odot]	1.572 ± 0.056 *
M_* [M_\odot]	1.306 ± 0.026 *
$\log_{10}(g)$ [cm/s 2]	4.161 ± 0.026 *
[Fe/H]	-0.19 ± 0.09 *
a/R_*	$7.27_{-0.44}^{+0.21}$
e	0 (fixed)
i [$^\circ$]	$87.96_{-1.56}^{+1.34}$
ω	0 (fixed)
P [days]	$3.7354845 \pm 1.9 \times 10^{-6}$ †
T_0 [BJD $_{TDB}$]	2454592.8015 ± 0.0005 †
R_p/R_*	$0.12229_{-0.00013}^{+0.00017}$
M_p [M $_\text{J}$]	0.477 ± 0.033 †
R_p [R $_\text{J}$]	1.932 ± 0.053 †

* Anderson et al. (2011)

† Southworth et al. (2012)

Two transits of the exoplanet were observed with the grisms G102 and G141, which cover the wavelengths between 0.8 - $1.1\ \mu\text{m}$ and 1.1 - $1.7\ \mu\text{m}$ respectively. We employed Iraclis (Tsiaras et al. 2016a), an open-source reduction pipeline for WFC3¹, to reduce the data and extract the lightcurves by performing the following steps: zero-read subtraction, reference pixels correction, non-linearity correction, dark current subtraction, gain conversion, sky background subtraction, calibration, flat-field correction, bad pixels and cosmic rays correction, and lightcurve extraction.

The WFC3 detector induces two different time-dependent systematics to the lightcurve: one exponential, at the beginning of each HST orbit, and one linear throughout the visit. Iraclis corrects for these systematics by fitting a transit fit model $F(t)$, computed using Pylightcurve, on the white lightcurve. $F(t)$ is a function of the limb-darkening coefficients, R_p/R_* and the orbital parameters T_0 , P , i , a/R_* , e , ω . The transit fit function is then multiplied by a normalisation factor n_w and a function $R(t)$ containing a linear and an exponential term as follows:

$$R(t) = (1 - r_a(t - T_0))(1 - r_{b1}e^{-r_{b2}(t - t_0)}) . \quad (1)$$

Here, t is time, T_0 is the mid-transit time, t_0 is the time when each orbit starts, r_a is the slope of the linear term and (r_{b1}, r_{b2}) are the coefficients of the expo-

¹ <https://github.com/ucl-exoplanets/Iraclis>

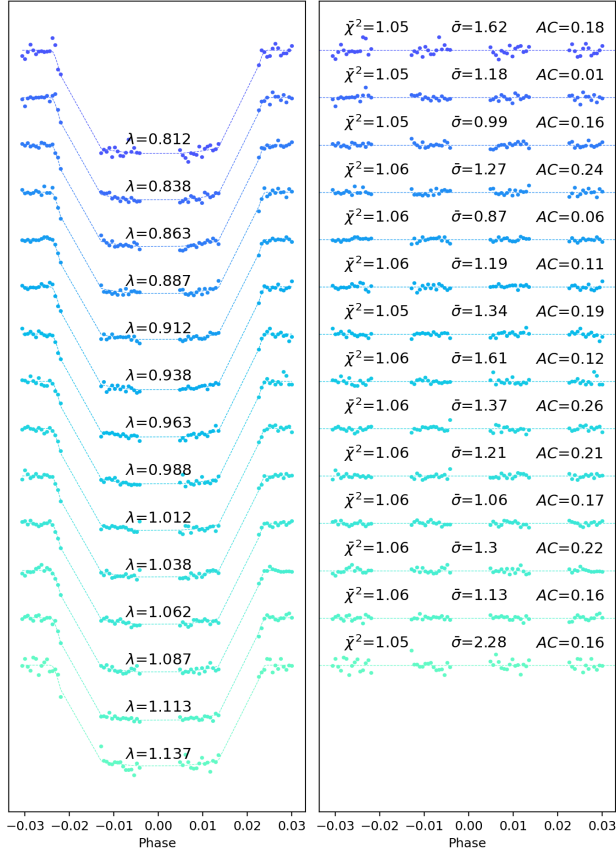
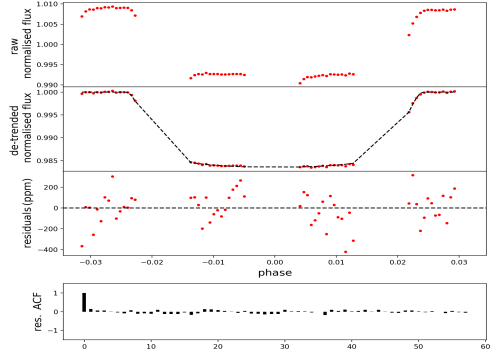
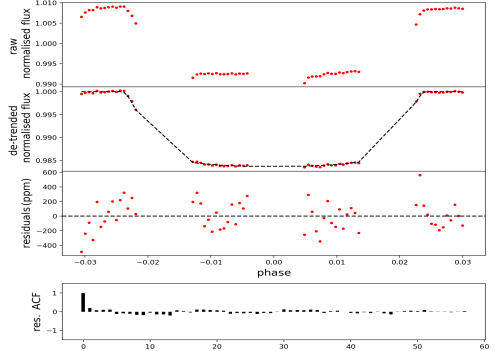


Figure 1. Top: white lightcurve for the HST/WFC3 G102 transmission observations of WASP-17b. First panel: raw lightcurve, after normalisation. Second panel: lightcurve, divided by the best fit model for the systematics. Third panel: residuals for best-fit model. Fourth panel: auto-correlation function of the residuals. Bottom: spectral lightcurves fitted with Iraclis for the HST/WFC3 G102 transmission spectra where, for clarity, an offset has been applied. Left panel: the detrended spectral lightcurves with the best-fit model plotted. Right panel: fitting residuals with values for the Chi-squared (χ^2), the standard deviation of the residuals with respect to the photon noise ($\bar{\sigma}$) and the auto-correlation (AC) of the residuals.

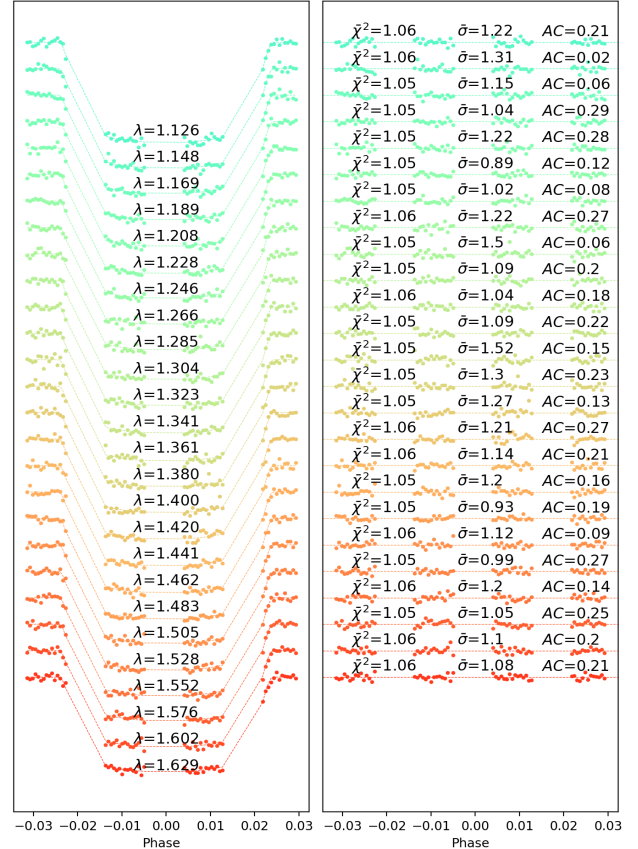


Figure 2. Top: white lightcurve for the HST/WFC3 G141 transmission observations of WASP-17b. First panel: raw lightcurve, after normalisation. Second panel: lightcurve, divided by the best fit model for the systematics. Third panel: residuals for best-fit model. Fourth panel: auto-correlation function of the residuals. Bottom: spectral lightcurves fitted with Iraclis for the HST/WFC3 G141 transmission spectra where, for clarity, an offset has been applied. Left panel: the detrended spectral lightcurves with the best-fit model plotted. Right panel: fitting residuals with values for the Chi-squared (χ^2), the standard deviation of the residuals with respect to the photon noise ($\bar{\sigma}$) and the auto-correlation (AC) of the residuals.

ential ramp. The spectral lightcurves are firstly fitted using Equation 1. Then, they are divided by the white lightcurve and further fitted via

$$n_\lambda(1 + \chi_\lambda(t - T_0))(F(\lambda, t)/F_w(t)) \quad (2)$$

where n_λ is a wavelength-dependent normalisation factor, χ_λ is the coefficient of the wavelength-dependent linear slope, t is time, T_0 is the mid-transit time, $F(\lambda, t)$ is the wavelength-dependent transit model and $F_w(t)$ is the best-fit model on the white lightcurve.

Further information on Iraclis can be found in Tsiaras et al. (2016a,b, 2018).

2.1.2. STIS

We downloaded the HST/STIS raw spectroscopic observations of WASP-17b from the Mikulski Archive for Space Telescopes (MAST), as part of the HST Proposal 12473 (P.I. David Sing).

Three transits of the exoplanet were observed with the gratings G430L (two transits) and G750L (one transit), which cover the wavelengths between 0.3 - 0.57 μm and 0.5 - 0.94 μm respectively. For the analysis of these datasets we used again Iraclis but adapted most of the reduction steps to STIS. These steps are: bias level subtraction, bias correction, image subtraction, dark image subtraction, flat field correction, calibration, background subtraction, bad pixels and cosmic rays correction, and lightcurve extraction. The first five steps were performed following the recipes described in the STIS Handbook (Bostroem & Proffitt 2011), while the rest were implemented in the same way as for the WFC3 staring-mode observations. For the extraction we used 6-pixel-wide apertures along the cross-dispersion direction and smoothed aperture edges along the dispersion direction (the smoothing factors were 5 \AA for the G430L grating and 10 \AA for the G750L grating, corresponding to approximately two pixels in each case).

2.2. HST lightcurve modelling

Table 1 summarises the parameters used for the lightcurve modelling. For these parameters we consulted the Exoplanet Characterisation Catalogue developed as part of the ExoClock project (Kokori et al. 2021). In all the lightcurve modelling steps we assumed a circular orbit and a fixed period for the planet, while the limb-darkening effect was modelled using the Claret 4-coefficient law (Claret 2000) and the ExoTETHyS (Morello et al. 2020) package which takes into account the stellar parameters (Table 1) and the response curve of the instrument.

At a first stage, the initial orbit of each HST visit was discarded since it presents more significant wavelength-

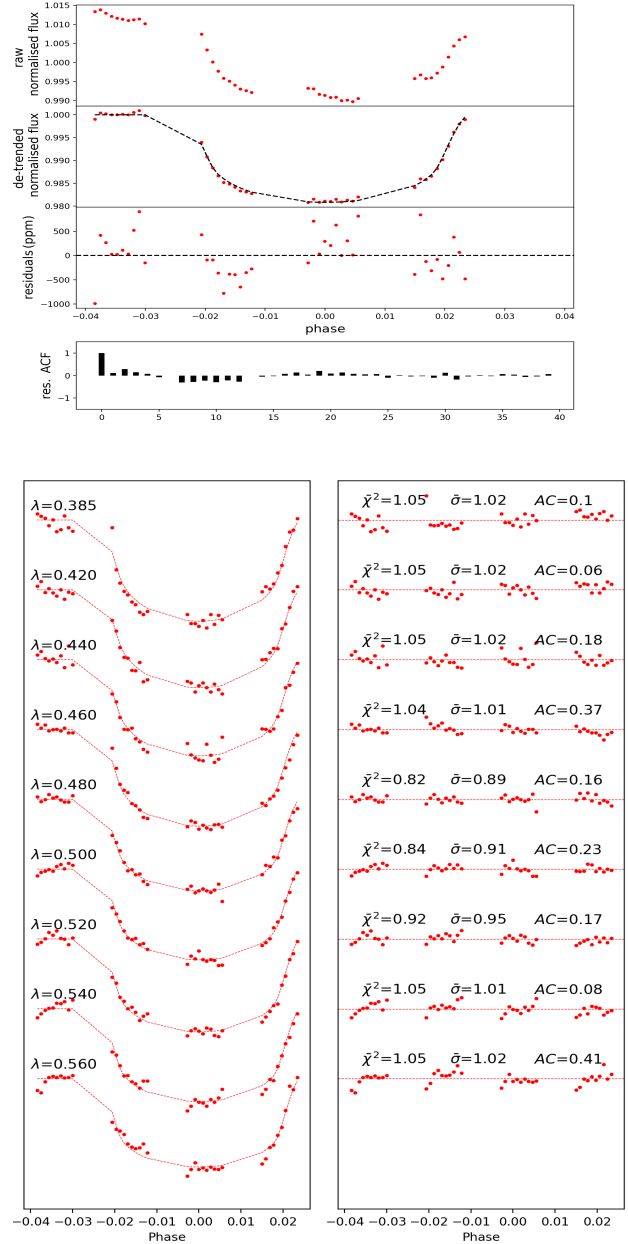


Figure 3. Top: white lightcurve for the HST/STIS G430L transmission observation taken on 2012-06-08 of WASP-17 b. First panel: raw lightcurve, after normalisation. Second panel: lightcurve, divided by the best fit model for the systematics. Third panel: residuals for best-fit model. Fourth panel: auto-correlation function of the residuals. Bottom: spectral lightcurves fitted with Iraclis for the same observation where, for clarity, an offset has been applied. Left panel: the detrended spectral lightcurves with the best-fit model plotted. Right panel: fitting residuals with values for the Chi-squared (χ^2), the standard deviation of the residuals ($\bar{\sigma}$) and the auto-correlation (AC) of the residuals.

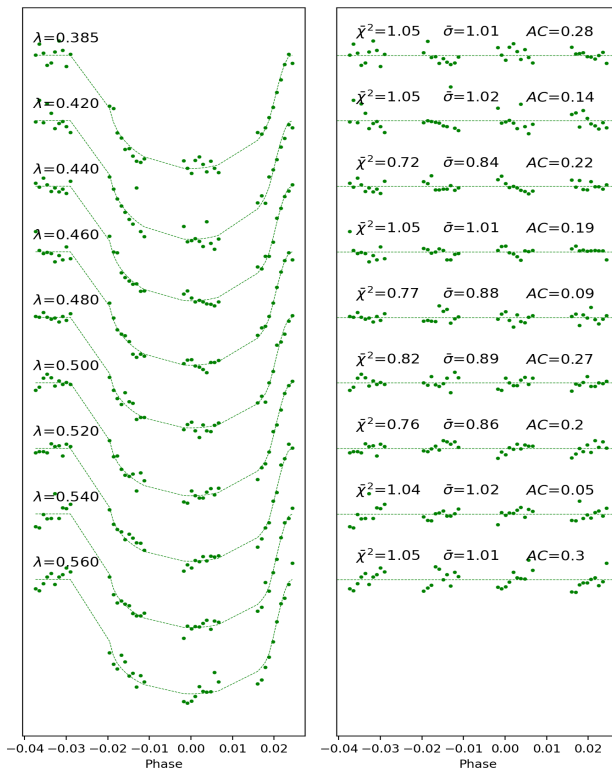
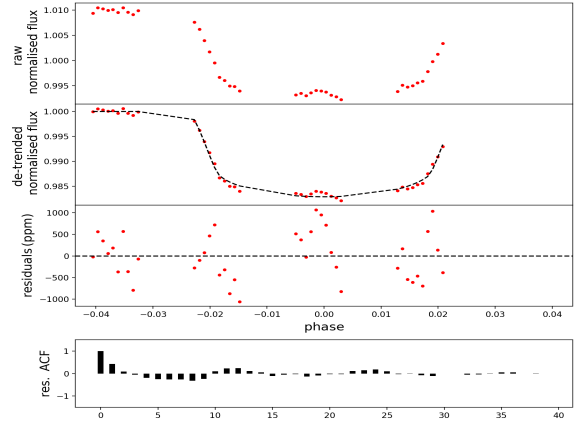
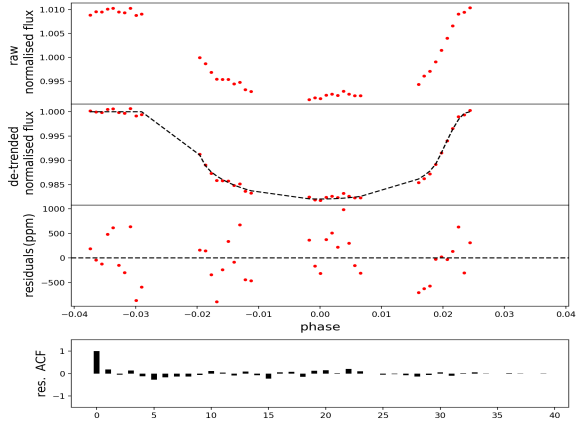


Figure 4. Top: white lightcurve for the HST/STIS G430L transmission observation taken on 2013-03-15 of WASP-17b. First panel: raw lightcurve, after normalisation. Second panel: lightcurve, divided by the best fit model for the systematics. Third panel: residuals for best-fit model. Fourth panel: auto-correlation function of the residuals. Bottom: spectral lightcurves fitted with Iraclis for the same observation where, for clarity, an offset has been applied. Left panel: the detrended spectral lightcurves with the best-fit model plotted. Right panel: fitting residuals with values for the Chi-squared (χ^2), the standard deviation of the residuals with respect to the photon noise ($\bar{\sigma}$) and the auto-correlation (AC) of the residuals.

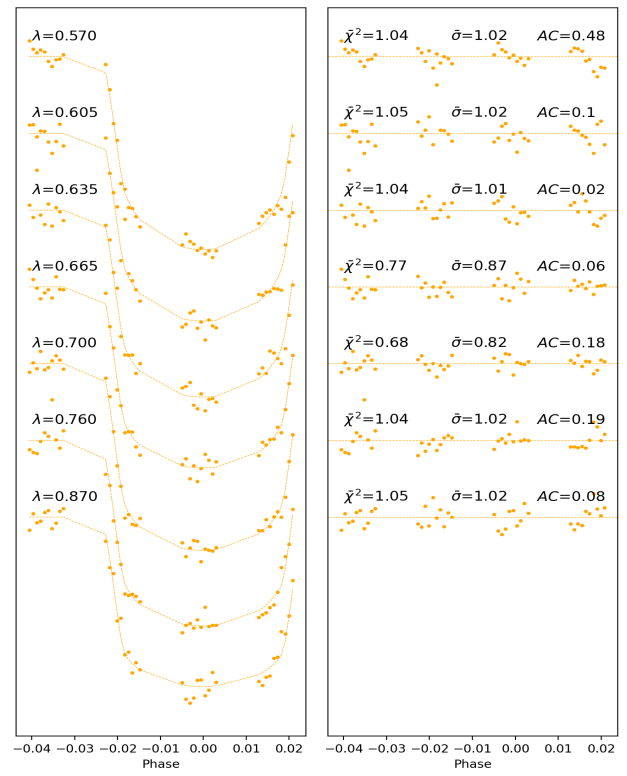


Figure 5. Top: white lightcurve for the HST/STIS G750L transmission observation taken on 2013-03-19 of WASP-17b. First panel: raw lightcurve, after normalisation. Second panel: lightcurve, divided by the best fit model for the systematics. Third panel: residuals for best-fit model. Fourth panel: auto-correlation function of the residuals. Bottom: spectral lightcurves fitted with Iraclis for the same observation where, for clarity, an offset has been applied. Left panel: the detrended spectral lightcurves with the best-fit model plotted. Right panel: fitting residuals with values for the Chi-squared (χ^2), the standard deviation of the residuals with respect to the photon noise ($\bar{\sigma}$) and the auto-correlation (AC) of the residuals.

dependent systematics compared to the subsequent orbits. We then analysed only the white lightcurves (broad-band) and let the semi-major axis, the inclination, the mid-transit time and the R_p/R_* as free parameters, together with a number of parameters for the systematics implemented in Iraclis.

To ensure consistency between the analysis of the different datasets, we estimated again the inclination and the semi-major axis of the planet using all the available data. We combined the lightcurves extracted from the five HST observations, together with five TESS (Ricker et al. 2014) observations. The updated parameters are reported in Table 1.

Finally, we analysed all the white and spectral HST lightcurves fixing the values for the semi-major axis and the inclination. Figures 1, 2, 3, 4 and 5 show the fitted white and spectral lightcurves for all the HST observations while Table 5 and 7 report the transmission data for STIS and WFC3 respectively.

2.3. Spitzer data analysis

Spitzer data is available on the IRSA online archive. We downloaded the WASP-17b transit observations taken with IRAC channel 1 and 2 in 2013 (P.I. Jean-Michel Desert, programme 90092). The two observations were analysed separately by employing the lightcurve detrending method named TLCD-LSTM² developed by Morvan et al. (2020). This approach uses a Long Short-Term Memory network (Hochreiter & Schmidhuber 1997) to predict the transit lightcurve without the need for any prior assumptions on the noise or transit shape. The only assumption regarding the systematics is that the associated correlated noise can be inferred from the out-of-transit lightcurve and the centroid time series. First, photometric lightcurves are extracted by using a circular aperture around the center of light. We tested a grid of radii apertures ranging from 2 to 4 pixels, by increment of 0.25 pixels. We then selected the aperture which maximised the signal-to-noise ratio, i.e. 3.25 pixels. We subtracted the background light computed at each time step using the median flux in each image after excluding a disk of radius 15 pixels around the source centre.

The neural network was then trained to learn the temporal variability on the pre-ingress and post-egress parts of the photometric lightcurve. While the stellar flux is masked during transit and then predicted autoregressively, the 2-D gaussian centroid time series is used as a covariate time series during the whole observation. This

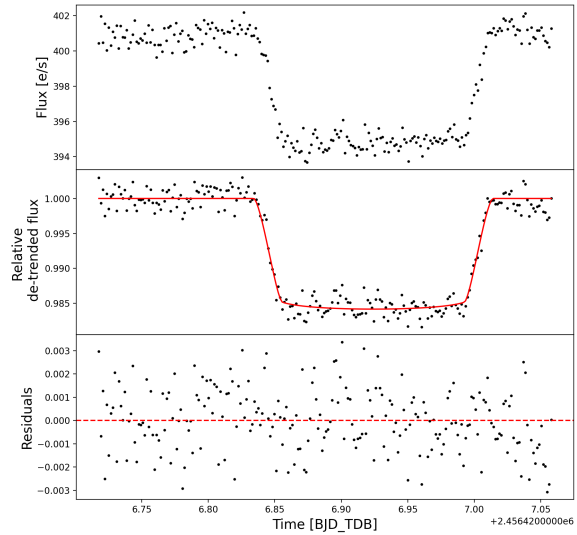
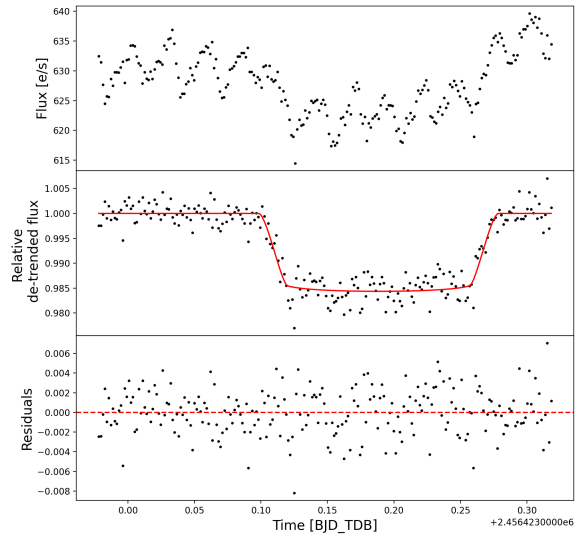


Figure 6. Raw lightcurves (first panel), detrended lightcurves (second panel) and residuals (third panel) for IRAC observations of WASP-17b with channel 1 (top) and 2 (bottom).

allows to leverage its correlations with the photometric lightcurve and infer the systematics during the transit while excluding the planetary signal. However, intermediate transit fits are performed during training on the temporary detrended lightcurve in order to keep track of the model's progress and provide an additional stopping criterion. A first run is done with large margins around the expected ingress and egress times to ensure that the

² <https://github.com/ucl-exoplanets/deepARTransit>

transits do not overlap with the training ranges. The margins are then refined after this first run to include 105% of the transit duration centered on the mid-transit time. In practice, the results are very stable and unaffected by the chosen margins provided these remain low (under $\approx 10\%$ of the transit duration). Several architecture and learning parameters are then tested. In both cases we find that 2 LSTM layers of 512 units and 10% dropout trained with an Adam optimiser and decay rate of $\beta = 0.95$ provide an optimal residual noise after the transit fit while avoiding overfitting. After the model was trained for 50 epochs, the best network - i.e. with the lowest residual noise - is saved along with the corresponding detrended lightcurve, obtained by dividing the raw lightcurve by the network's prediction. A final transit fit is performed using a Markov Chain Monte Carlo procedure embedded in the PyLightcurve package (Tsiaras et al. 2016a). Both during and after training, the fixed planetary parameters used are those listed in Table 1 or computed using the ExoTETHyS open package (Morello et al. 2020) while the mid-transit time and R_p/R_* were let free. The full list of parameters used to train the network is available in Table 4.

The raw and detrended Spitzer lightcurves are shown in Figure 6 (top: IRAC channel 1; bottom: IRAC channel 2) and the corresponding transmission data is available in Table 6.

2.4. Atmospheric Modelling

The spectrum resulting from our data reduction process is shown in Figure 7. Each STIS dataset is indicated with a different colour depending on the date the observation was taken on. WFC3 and Spitzer data are shown in blue and purple respectively, independently of the grism or channel employed. From the aforementioned plot we can easily notice divergent results coming from the two STIS/G430L observations, namely those taken on 2012-06-08 and 2013-03-15. For this reason we decided to model the observed spectrum in three separate scenarios. Case 1 includes STIS visits 2012-06-08 (visit 1) and 2013-03-19 (visit 3), WFC3 and Spitzer data while in Case 2 we aimed to model STIS visits 2013-03-15 (visit 2) and 2013-03-19 (visit 3), WFC3 and Spitzer datasets. Additionally, we investigated the spectrum constituted by the WFC3 observations only (Case 3), thus discarding the inconsistencies of the STIS observations.

In Figure 7 we compare our data with the analysis from Sing et al. (2016). We observe that our STIS visit 1, STIS visit 3, WFC3/G141 and Spitzer data agree with the previous analysis by Sing et al. (2016), finding however an inconsistency with the data point at $0.6\ \mu\text{m}$.

Additionally, we notice that our STIS visit 2 data do not have a counterpart in the analysis by Sing et al. (2016), although their study claims to have analysed all STIS observations available. We believe that their approach consisted in performing a weighted average of STIS visit 1+2, but we cannot be sure as this information is not included in their methodology.

In each spectral case, we modelled the atmosphere at the terminator of WASP-17b using the open-source atmospheric retrieval framework TauREx 3 (Al-Refaei et al. 2021). As it is customary for hot-Jupiters, we assumed this exoplanetary atmosphere to be mainly constituted by H_2 and He in a ratio of 0.17. Given the short orbital period and an unconstrained eccentricity, we expect a tidally-locked exoplanet with an equilibrium temperature that remains constant throughout the whole orbit around the host star. Using the equation

$$T_p = T_* \sqrt{\frac{R_*}{2a}} \left(\frac{1-A}{\epsilon} \right)^{\frac{1}{4}}, \quad (3)$$

we estimated the equilibrium temperature to be $T_p = 1769\ \text{K}$ when assuming $A = 0.1$ and $\epsilon = 0.8$. However, since we cannot ascertain the exact albedo and emissivity of the planet, we considered some extreme cases which produce a range where we expect the planetary temperature to fall. For instance, if we assume WASP-17b to possess an albedo of 0.5 and an emissivity of 0.7 (analogue to Jupiter), the planetary equilibrium temperature suddenly drops to $T_p = 1579\ \text{K}$. If instead we consider the case of a planet that reflects a tiny amount of incoming light ($A = 0.1$) and re-emits some energy (possibly energy left over from the planet's formation process) with $\epsilon = 0.7$, then the equilibrium temperature increases to $T_p = 1829\ \text{K}$.

As a result of the broad wavelength coverage of the combined observations and the high planetary equilibrium temperature (Sharp & Burrows 2007), we explored the presence of a variety of molecular opacities, ranging from the optical (TiO (McKemmish et al. 2019), VO (McKemmish et al. 2016), FeH (Dulick et al. 2003; Wende et al. 2010), SiH (Yurchenko et al. 2018), TiH (Gharib-Nezhad et al. 2021), AlO (Patrascu et al. 2015), K (Allard et al. 2019) and Na (Allard et al. 2019)), to the near-infrared and infrared absorbers (H_2O (Polyansky et al. 2018), CH_4 (Yurchenko & Tennyson 2014), CO (Li et al. 2015), CO_2 (Rothman et al. 2010) and NH_3 (Coles et al. 2019)), by employing the linelists from the ExoMol (Tennyson et al. 2016; Chubb et al. 2021), HITEMP (Rothman et al. 2010; Rothman & Gordon 2014), HITRAN (Gordon et al. 2016; Rothman et al. 1987) and NIST (Kramida 2013) databases.

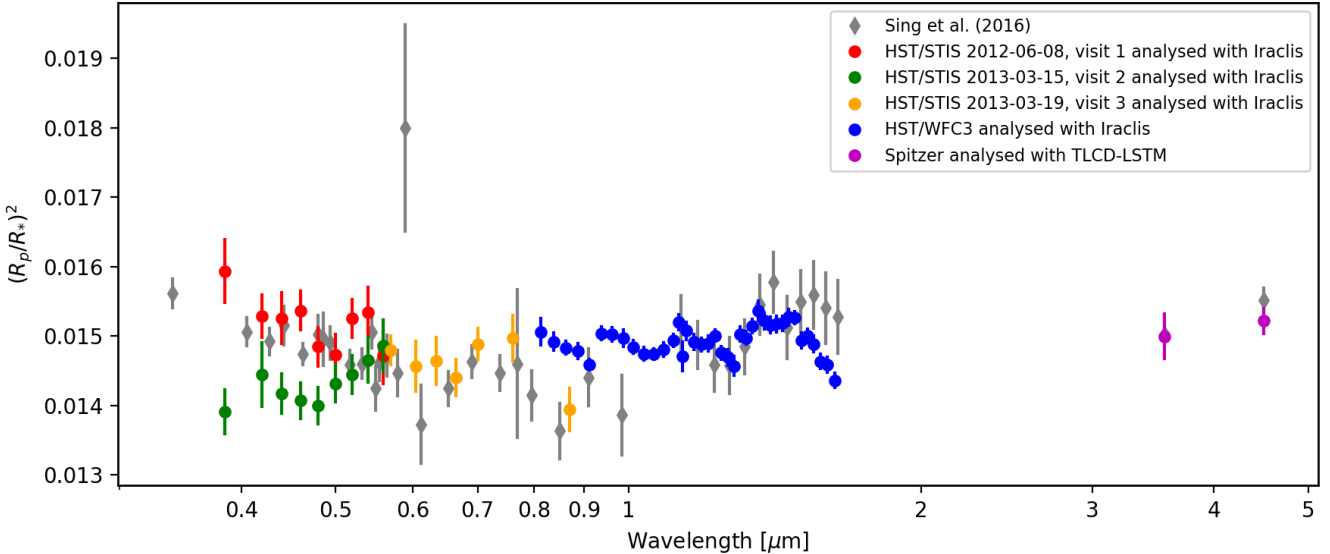


Figure 7. Transmission spectrum of WASP-17 b, constituted by HST/STIS, HST/WFC3 and Spitzer/IRAC channel 1 and 2 data analysed in this study compared to the data from Sing et al. (2016).

In our final retrievals we considered only the presence of H₂O, AlO, TiH, SiH, CO, CH₄ as trace gases. The molecular profile of each species was set to be constant at each atmospheric layer. Additionally, collision Induced Absorption (CIA) from H₂-H₂ (Abel et al. 2011; Fletcher et al. 2018) and H₂-He (Abel et al. 2012), Rayleigh scattering for all molecules and the presence of gray clouds and hazes modelled with the Lee et al. (2013) parameterisation were included. We also modelled the contamination of the host star on the spectrum of WASP-17 b using the formalisation by Rackham et al. (2018, 2019).

We assumed a planetary atmosphere constituted by 100 layers in a plane-parallel geometry, uniformly distributed in log space between 10⁻⁵ and 10⁶ Pa. The temperature structure was modelled with an isothermal $T - p$ profile. The trace gases considered were allowed to vary freely between 10⁻¹² and 10⁻¹ in volume mixing ratio, while the planetary equilibrium temperature, T_p , could vary between 500 and 3000 K. Regarding the hazes, their top pressure P_{Mie}^{top} ranged from 10⁻⁴ to 10⁶ Pa, the radius of the particles R_{Mie}^{Lee} between 10⁻³ and 1 μm and the Mie cloud mixing ratio χ_{Mie}^{Lee} could change between -30 and -4 in log-space. Furthermore, we included a layer of gray clouds, whose top pressure could vary between 10⁻¹ and 10⁶ Pa (Robinson & Catling 2014; Kawashima & Ikoma 2018; Charnay et al. 2021). Lastly, the planetary radius bounds were set between 1 and 2 R_J . The prior bounds employed for each fitted parameter are reported in Table 2.

We investigated the parameter space with the nested sampling algorithm MultiNest (Feroz et al. 2009b) with 750 live points and an evidence tolerance of 0.5.

2.5. Stellar Modelling

We attempted to explain the steep downward slope in the blue wavelengths of STIS visit 2 observation (see Figure 7) by modelling the effect of a combination of unocculted stellar spots and faculae on the Case 2 transmission spectrum of WASP-17 b. We accounted for solar size spots and faculae to be homogeneously distributed on the stellar surface. Current stellar models and observational evidence (Rackham et al. 2019, 2017; Mamajek & Hillenbrand 2008; Ciardi et al. 2011) show that the variability of F-dwarfs is $\sim 0.1\%$, with a minimum of 0.07% and a maximum of 0.36%. This is one of the lowest among all stellar spectral types, with the stellar variability being inversely proportional to the temperature of the star (McQuillan et al. 2014). Though generally FGK stars are mostly inactive and do not contaminate the transmission spectrum of the planets orbiting them, their active counter-parts do, and great care must be taken when analysing the planetary spectra that they pollute.

According to Rackham et al. (2019), for FGK-type stars the stellar spot temperature can be calculated as:

$$T_{spot} [K] = 0.418 T_{phot} + 1620 \quad (4)$$

and the faculae temperature as:

$$T_{fac} [K] = T_{phot} + 100 , \quad (5)$$

with T_{phot} being the temperature of the stellar photosphere, in our study equal to 6550 ± 80 K. The spectral emission density of the heterogeneous star is modelled using the BT-Settl models (Allard et al. 2013) and the stellar spectral model grid is generated using the PHOENIX library (Husser et al. 2013). In essence, the spots and faculae are modelled as separate cooler and hotter stars respectively (Thompson et al. (in prep)). The stellar emission densities (SEDs) of the three surface components (spots, faculae and quiescent photosphere) are then combined in the ratio of their covering fractions to produce the observed disk-integrated stellar spectrum

$$S_{star,\lambda} = ((1 - F_{spot} - F_{fac}) \times S_{phot,\lambda}) + (F_{spot} \times S_{spot,\lambda}) + (F_{fac} \times S_{fac,\lambda}), \quad (6)$$

where $S_{star,\lambda}$ is the flux of the heterogeneous star at a given wavelength, $S_{phot,\lambda}$, $S_{spot,\lambda}$ and $S_{fac,\lambda}$ are the spectra of the quiet photosphere, the starspots and the faculae at the same wavelength respectively and F_{spot} and F_{fac} are the covering fractions of the spots and faculae with respect to the observed stellar disk.

Compared to the nominal transit depth, the effect of an heterogeneous star produces a wavelength-dependent offset on the transmission spectrum given by

$$\epsilon_{\lambda,s+f} = \frac{1}{1 - F_{spot} \left(1 - \frac{S_{\lambda,spot}}{S_{\lambda,phot}} \right) - F_{fac} \left(1 - \frac{S_{\lambda,fac}}{S_{\lambda,phot}} \right)}, \quad (7)$$

where F_{spot} and F_{fac} are the covering fractions of the spots and faculae and $S_{\lambda,spot}$, $S_{\lambda,fac}$ and $S_{\lambda,phot}$ are the emitted fluxes of the spots, faculae and immaculate photosphere at a given wavelength respectively. An important limitation to consider is that this simplistic method of modelling stellar active regions may be inaccurate, particularly with respect to faculae modelling as it fails to describe any centre-to-limb variations that they may exhibit or their strong dependence on magnetic field strength (Norris et al. 2017). However, given the precision of the observations in question this simplified stellar model should be sufficient to begin to investigate any potential heterogeneity displayed by WASP-17.

In our retrievals, we considered a varying spot temperature between 4000 and 5000 K, and a faculae temperature between 6600 and 7000 K. Both the spots and faculae coverage fraction bounds were set between 0.0 and 0.9 of the total stellar surface.

We tested the possibility of a variable stellar photosphere also on the spectrum in Case 1 and Case 3.

3. RESULTS

3.1. Retrievals accounting for an active star

When comparing the posteriors for each of the three cases in Figure 8, one can find common atmospheric features that are stable independently of the datasets modelled. Firstly, the planetary temperatures retrieved are within 1σ of each other and their upper bounds are inside the limits of the equilibrium temperature [1579 K; 1829 K] calculated in Section 2.4. Similarly, the planetary radii at 10 bar are compatible with one another.

All three spectra agree on a number of aspects: the presence of water in the solar/super-solar regime which is consistent with the result from Pinhas et al. (2018), $\log_{10}(\text{H}_2\text{O}) = -4.04^{+0.91}_{-0.42}$. The reference solar water abundance, was calculated under thermochemical equilibrium at a pressure of 1 bar for the equilibrium temperature of WASP-17b and it is equal to $\log_{10}(\text{X}_{\text{H}_2\text{O}}) = -3.3$ (Pinhas et al. 2018).

Our results suggest the presence of AlO and TiH in the order of 10^{-8} in volume mixing ratio, unconstrained SiH and hazes non-detection. Furthermore the retrievals indicate a strong stellar contamination on the spectrum of WASP-17b, in the WFC3 dataset too where we do not expect stellar activity to play a big part. In all three scenarios we retrieved a spot temperature around 4300 K, as well as spots and faculae covering fraction of the star in the order of 10-20% and 40-50% respectively. Our results report a faculae temperature in the Case 1 transmission spectrum between 33 and 165 K higher than what Equation 5 predicts. On the other hand, T_{fac} on Case 2 and Case 3 spectra results between 217 and 322 K higher than expected ($T_{fac}=6919.28^{+53.01}_{-40.73}$ and $T_{fac}=6914.43^{+55.02}_{-47.08}$). Although the study by Rackham et al. (2018) does not provide typical uncertainties on the temperature of spots and faculae, we can easily compare the retrieved values with the stellar photospheric uncertainty (~ 80 K) from Table 1. Hence, the T_{fac} retrieved in Case 1, being less than 2σ away from the 80 K uncertainty, could be deemed acceptable compared to the faculae temperature in Case 2 and 3, which is three to four times above the 80 K limit.

In Case 2 and Case 3 spectra we find super-solar water abundances ($\log_{10}(\text{H}_2\text{O})=-1.93^{+0.39}_{-0.70}$ and $\log_{10}(\text{H}_2\text{O})=-2.19^{+0.55}_{-0.69}$ respectively), while Case 1 returns a $\log_{10}(\text{H}_2\text{O})=-3.20^{+0.99}_{-0.60}$, being $0.97 \times$ solar and 0.79 times the result reported by Barstow et al. (2016), equal to 5×10^{-4} . Depending on the spectral scenario considered, the AlO, TiH and SiH abundances retrieved differ (Case 1: $\log_{10}(\text{AlO})=-7.94^{+0.87}_{-0.81}$, $\log_{10}(\text{TiH})=-9.70^{+1.01}_{-1.14}$, $\log_{10}(\text{SiH})=-8.39^{+2.25}_{-2.21}$; Case 2: $\log_{10}(\text{AlO})=-9.68^{+1.55}_{-1.42}$, $\log_{10}(\text{TiH})=-7.91^{+0.98}_{-1.00}$, $\log_{10}(\text{SiH})=-7.03^{+2.24}_{-2.84}$; Case 3: $\log_{10}(\text{AlO})=-6.39^{+0.81}_{-1.41}$, $\log_{10}(\text{TiH})=-7.82^{+1.10}_{-1.59}$, $\log_{10}(\text{SiH})=-7.08^{+3.02}_{-3.05}$), yet they are compatible with one another being within

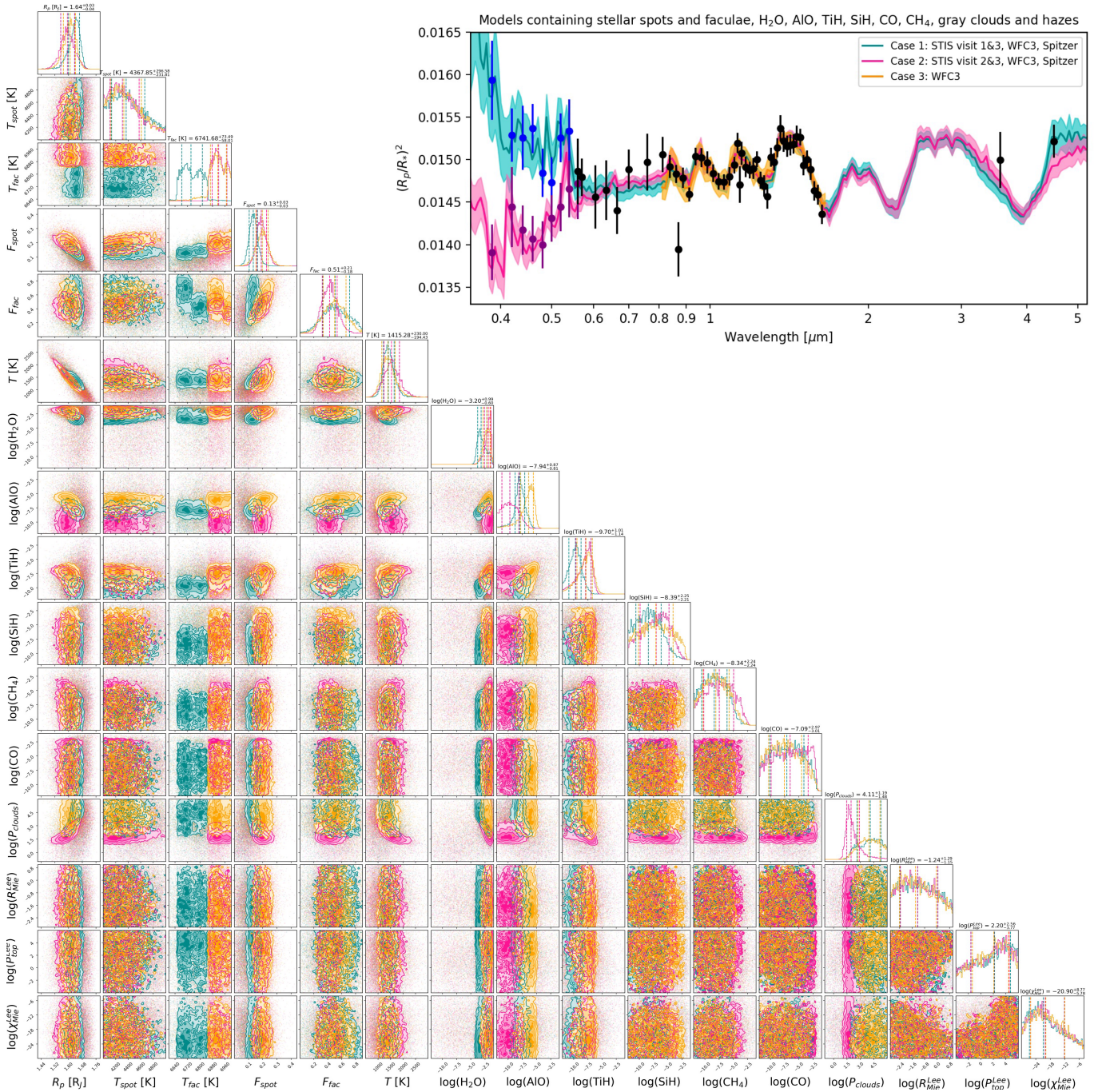


Figure 8. Posterior distributions for the transmission spectrum of WASP-17b accounting for an active star retrieved with different datasets. The dashed vertical lines in each histogram refer to the median value, the first quantile (lower bound error) and the third quantile (upper bound error) of each parameter. Similarly, the reported values on top of the histograms denote the parameter’s median value, the first and the third quantile. The values shown are those obtained with the spectrum constituted by STIS visit 1&3, WFC3, Spitzer (Case 1). Inset: transmission spectra with best-fit models and their 1σ uncertainties.

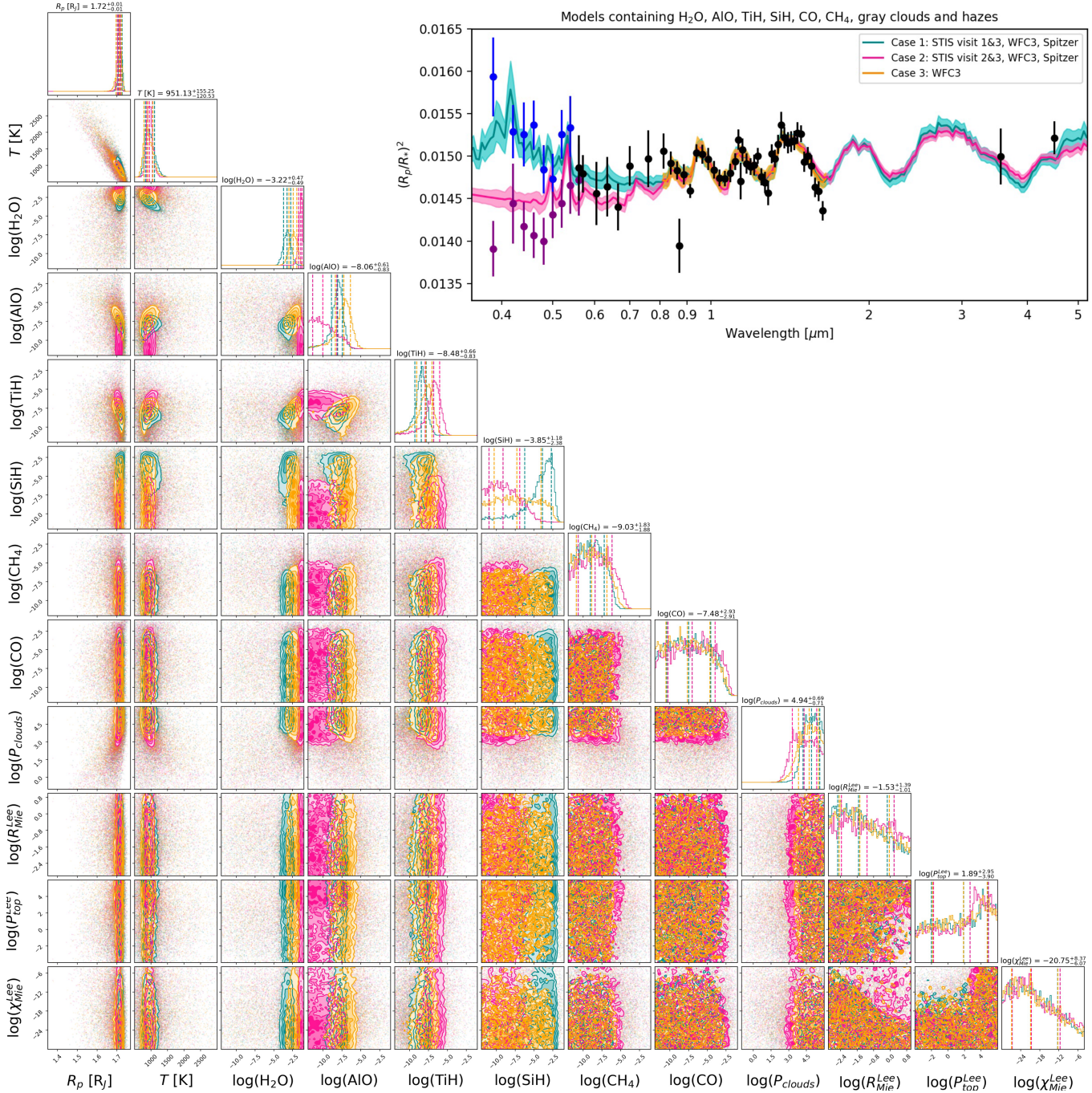


Figure 9. Posterior distributions for the transmission spectrum of WASP-17 b accounting for a homogeneous star retrieved with different datasets. The dashed vertical lines in each histogram refer to the median value, the first quantile (lower bound error) and the third quantile (upper bound error) of each parameter. Similarly, the reported values on top of the histograms denote the parameter’s median value, the first and the third quantile. The values shown are those obtained with the spectrum constituted by STIS visit 1&3, WFC3, Spitzer (Case 1). Inset: transmission spectra with best-fit models and their 1σ uncertainties.

their 1σ confidence band. According to the thermochemical equilibrium model GGChem (Woitke et al. 2018), the expected abundance of AlO and TiH at $p=1$ bar and $T=\sim 1400$ K is $\sim 10^{-11}$ and $\sim 10^{-12}$ in VMR respectively. The theoretical estimate is in accordance with the retrieved AlO abundance in Case 2, where we find a lower bound equal to $\log_{10}(\text{AlO})=-11.1$. However, in all other cases for both AlO and TiH, the retrieved abundances are 3 to 4 sigmas away from the expected values. On the contrary, the retrieved uncertainties on the SiH abundances are in agreement with the theoretical value computed at $p=1$ bar and $T=\sim 1400$ K, it being $\log_{10}(\text{SiH})=\sim -10$.

We retrieve conflicting results for the cloud deck. The Case 1 and Case 3 posteriors returned a mean cloud deck at a pressure of $\sim 1.1 \times 10^4$ Pa corresponding to ~ 0.11 bar. In Case 2 the clouds top pressure is higher in the atmosphere, at a pressure of 0.9 mbar. The cloud coverage found at higher altitudes could be caused by the retrieval framework trying to fit the downward slope created by the STIS visit 2 data in the optical range, which cannot be explained by any molecular absorber. The clouds cut off any molecular signature in the optical, leaving just the tip of two particular TiH and SiH signatures visible at 0.54 and 0.42 μm in the Case 2 spectrum.

Figure 10 shows Case 1 data fitted by the best-fit model accounting for stellar activity and the contributions of active trace gases, CIA, clouds and hazes to the fit.

We report the retrieval results for each spectral case in Table 2 (upper part).

3.2. Retrievals accounting for a homogeneous star

We modelled the three spectral scenarios previously identified by accounting for the same molecular and atmospheric parameters. However, in this instance we modelled the star as a homogeneous body. We find that the absence of stellar activity does not impact the molecular detections, but it does affect a few of the retrieved abundances.

As in the previous case, our data suggests the presence of water, aluminium oxide and titanium hydride. Our retrievals return solar $\log_{10}(\text{H}_2\text{O})=-3.22^{+0.47}_{-0.49}$ and super-solar $\log_{10}(\text{H}_2\text{O})=-2.41^{+0.48}_{-0.56}$, $\log_{10}(\text{H}_2\text{O})=1.40^{+0.19}_{-0.28}$ water concentrations when modelling the Case 1, Case 3 and Case 2 spectrum respectively. The latter two results indicate a higher abundance than what current theories predict for hot-Jupiters ($\log_{10}(\text{H}_2\text{O})=\sim 3.3$) (Venot et al. 2012; Venot & Agúndez 2015; Woitke et al. 2018).

The AlO and TiH abundances retrieved from the Case 3 spectrum appear to be more compatible to those re-

trieved from Case 1. However, both the AlO and the TiH results obtained from each of the three cases are within their respective 1σ uncertainties. These results are not consistent with chemical equilibrium models, as Woitke et al. (2018) predict a volume mixing ratio of roughly 10^{-16} for AlO and 10^{-18} for TiH at a pressure of 1 bar and $T=\sim 900$ K. The discrepancies could be caused by chemical disequilibrium processes, e.g. photochemistry (Venot et al. 2015; Fleury et al. 2019) or quenching (Shulyak et al. 2020), occurring in the atmosphere of WASP-17b.

SiH is still largely undetected in Case 2 and Case 3 spectrum. On the other hand, exceptionally high amounts of this trace gas are detected in Case 1. We recognise that such large contribution ($\log_{10}(\text{SiH})=-3.85^{+1.18}_{-2.38}$) is unlikely as theoretical models (Woitke et al. 2018) predict a SiH volume mixing ratio of $\sim 10^{-16}$ at 1 bar and at ~ 900 K. Moreover, all three spectra return a consistent median planetary radius, temperature and cloud coverage, approximately equal to $1.71 R_J$, 930 K and $\sim 4.6 \times 10^4$ Pa respectively.

In place of stellar faculae, a Mie scattering haze could have explained the upward slope in Case 1 spectrum. Unfortunately, this option is refused by the retrieval, which is not able to constrain any of the aerosol parameters: particle size R_{Mie}^{Lee} , top pressure P_{Mie}^{top} , mixing ratio χ_{Mie}^{Lee} . Even when we test the aerosols presence in the simplest model containing only water and clouds, their posterior distributions are completely unconstrained.

The retrieved values for each atmospheric parameter are reported in Table 2 (bottom part) while Figure 11 shows Case 2 data fitted by the best-fit model and the contributions of active trace gases, CIA, clouds and hazes to the fit.

4. DISCUSSION

WASP-17b has been observed, studied and modelled intensively in the past, e.g. Anderson et al. (2011); Mandell et al. (2013); Pinhas et al. (2018); Goyal et al. (2020), by employing observations taken with WFC3/G141 (staring mode), HST/STIS and Spitzer. Our study, complementary to the work by Alderson et al. (2022), offers a consistent analysis performed by combining and reducing in a reproducible manner all currently available WASP-17b transmission data obtained with space-based observatories. We include all public STIS and IRAC data, plus WFC3/G141 and WFC3/G102 observations both taken in spatial scanning mode. This large breadth of observations allows us to investigate the planet's atmospheric spectrum spanning the wavelengths from the optical to the near infrared.

Table 2. List of the parameters, their prior bounds, the scale used and the retrieved values (median and standard deviation) for the Case 1, Case 2 and Case 3 spectra assuming an isothermal atmospheric profile.

Retrieval accounting for an active star

Retrieved parameters	Prior bounds	Scale	Case 1	Case 2	Case 3
			STIS 1&3, WFC3, IRAC	STIS 2&3, WFC3, IRAC	WFC3
R_p [R _J]	1 ; 2	linear	$1.64^{+0.03}_{-0.04}$	1.59 ± 0.04	$1.61^{+0.03}_{-0.04}$
T_{spot} [K]	4000 ; 5000	linear	$4367.85^{+296.58}_{-231.81}$	$4306.83^{+267.22}_{-196.70}$	$4329.70^{+278.98}_{-206.75}$
T_{fac} [K]	6600 ; 7000	linear	$6741.68^{+73.49}_{-58.01}$	$6919.28^{+53.01}_{-40.73}$	$6914.43^{+55.02}_{-47.08}$
F_{spot}	0.0 ; 0.9	linear	0.13 ± 0.03	$0.19^{+0.04}_{-0.03}$	0.20 ± 0.04
F_{fac}	0.0 ; 0.9	linear	$0.51^{+0.21}_{-0.18}$	$0.43^{+0.11}_{-0.10}$	0.50 ± 0.16
T [K]	500 ; 3000	linear	$1415.28^{+230}_{-194.43}$	$1539.70^{+317.21}_{-304.42}$	$1396.20^{+291.34}_{-243.79}$
H ₂ O	-12 ; -1	log ₁₀	$-3.20^{+0.99}_{-0.60}$	$-1.93^{+0.39}_{-0.70}$	$-2.19^{+0.55}_{-0.69}$
AlO	-12 ; -1	log ₁₀	$-7.94^{+0.87}_{-0.81}$	$-9.68^{+1.55}_{-1.42}$	$-6.39^{+0.81}_{-1.41}$
TiH	-12 ; -1	log ₁₀	$-9.70^{+1.01}_{-1.14}$	$-7.91^{+0.98}_{-1.70}$	$-7.82^{+1.10}_{-1.59}$
SiH	-12 ; -1	log ₁₀	$-8.39^{+2.25}_{-2.21}$	$-7.03^{+2.24}_{-2.84}$	$-7.08^{+3.02}_{-3.05}$
CH ₄	-12 ; -1	log ₁₀	-8.34 ± 2.24	$-7.48^{+2.55}_{-2.72}$	$-8.08^{+2.34}_{-2.24}$
CO	-12 ; -1	log ₁₀	$-7.09^{+2.97}_{-3.01}$	$-6.51^{+3.15}_{-3.36}$	$-7.55^{+3.03}_{-2.77}$
P_{clouds} [Pa]	-1 ; 6	log ₁₀	$4.11^{+1.19}_{-1.48}$	$1.95^{+0.48}_{-0.93}$	$3.98^{+1.33}_{-1.03}$
R_{Mie}^{Lee} [μm]	-3 ; 1	log ₁₀	$-1.24^{+1.29}_{-1.15}$	$-1.25^{+1.29}_{-1.10}$	$-1.38^{+1.33}_{-1.03}$
P_{Mie}^{top} [Pa]	-4 ; 6	log ₁₀	$2.20^{+2.56}_{-3.77}$	$2.11^{+2.44}_{-3.71}$	$2.08^{+2.36}_{-3.42}$
χ_{Mie}^{Lee}	-30 ; -4	log ₁₀	$-20.90^{+8.77}_{-5.78}$	$-20.13^{+8.06}_{-6.07}$	$-19.87^{+7.91}_{-6.27}$

Retrieval accounting for a homogeneous star

Retrieved parameters	Prior bounds	Scale	Case 1	Case 2	Case 3
			STIS 1&3, WFC3, IRAC	STIS 2&3, WFC3, IRAC	WFC3
R_p [R _J]	1 ; 2	linear	1.72 ± 0.01	1.71 ± 0.01	$1.71^{+0.01}_{-0.02}$
T [K]	500 ; 3000	linear	$951.13^{+155.25}_{-120.53}$	$950.73^{+93.36}_{-83.04}$	$900.56^{+153.18}_{-112.25}$
H ₂ O	-12 ; -1	log ₁₀	$-3.22^{+0.47}_{-0.49}$	$-1.40^{+0.19}_{-0.28}$	$-2.41^{+0.48}_{-0.56}$
AlO	-12 ; -1	log ₁₀	$-8.06^{+0.61}_{-0.83}$	$-10.03^{+1.86}_{-1.35}$	$-7.25^{+0.87}_{-1.12}$
TiH	-12 ; -1	log ₁₀	$-8.48^{+0.66}_{-0.83}$	$-6.83^{+0.79}_{-1.11}$	$-7.85^{+0.82}_{-1.22}$
SiH	-12 ; -1	log ₁₀	$-3.85^{+1.18}_{-2.38}$	$-9.10^{+2.23}_{-1.87}$	$-7.26^{+3.20}_{-3.04}$
CH ₄	-12 ; -1	log ₁₀	$-9.03^{+1.83}_{-1.88}$	$-8.40^{+2.24}_{-2.26}$	-8.87 ± 2.04
CO	-12 ; -1	log ₁₀	$-7.48^{+2.93}_{-2.91}$	$-7.03^{+3.08}_{-3.21}$	$-7.64^{+3.00}_{-2.87}$
P_{clouds} [Pa]	-1 ; 6	log ₁₀	$4.94^{+0.69}_{-0.71}$	$4.31^{+1.06}_{-1.00}$	$4.74^{+0.80}_{-0.91}$
R_{Mie}^{Lee} [μm]	-3 ; 1	log ₁₀	$-1.53^{+1.39}_{-1.01}$	$-1.12^{+1.31}_{-1.24}$	$-1.47^{+1.43}_{-1.01}$
P_{Mie}^{top} [Pa]	-4 ; 6	log ₁₀	$1.89^{+2.95}_{-3.90}$	$2.67^{+2.22}_{-4.42}$	$1.87^{+2.88}_{-3.75}$
χ_{Mie}^{Lee}	-30 ; -4	log ₁₀	$-20.75^{+8.37}_{-6.07}$	$-20.63^{+9.05}_{-6.04}$	$-20.88^{+8.56}_{-6.01}$

The combination of several datasets has its pros and cons. By coupling observations taken at different wavelengths, we are able to achieve a broad wavelength coverage, paramount to obtain more precise measurements and unambiguous molecular detection. It is extremely challenging to absolutely calibrate data obtained from different detectors, especially if each of them targets a very specific spectral range with a limited or even absent wavelength overlap (Yip et al. 2020). Moreover, each instrument creates its own distinct systematics that need to be modelled ad hoc.

The STIS detector shares a short portion of the wavelength space, about 0.14 μm, with WFC3. This wavelength overlap is useful to investigate potential calibration discrepancies between instruments. In the 0.8-0.94 μm range, our spectrum displays six WFC3/G102 datapoints and one STIS/G750L point (Fig. 7). The response of the STIS G750L grating shows a strong dip above 0.8 μm (Prichard et al. 2022), hence the last spectral bin (0.8-0.94 μm) has a flux rate ~50% lower than the rest of the bands and it is possibly subject to different systematics. Because of the shape of the transmission curve, we opted to increase the size of the final

Table 3. Bayesian log-difference between different models depending on the observations fed to the retrievals.

Case 1: STIS visit 1&3, WFC3, Spitzer				
Setup	Log Evidence	Sigma (discarded by)	Retrieved Temperature [K]	
(1) H ₂ O, AlO, TiH, SiH, CH ₄ , CO, clouds, hazes, stellar activity	395.73		1415.28 ^{+230.00} _{-194.43}	
(2) H ₂ O, AlO, TiH, SiH, CH ₄ , CO, clouds, hazes	389.31	4.01 w.r.t. (1)	951.13 ^{+155.25} _{-120.53}	
(3) H ₂ O, clouds, stellar activity	395.02	1.84 w.r.t. (1)	1429.50 ^{+363.20} _{-245.74}	
(4) H ₂ O, AlO, TiH, SiH, clouds, hazes, stellar activity	395.90	< 1 w.r.t. (1)	1397.57 ^{+229.83} _{-193.95}	
(5) H ₂ O, TiO, VO, FeH, clouds, stellar activity	393.60	2.6 w.r.t. (1)	1854.96 ^{+382.33} _{-495.03}	

Case 2: STIS visit 2&3, WFC3, Spitzer				
Setup	Log Evidence	Sigma (discarded by)	Retrieved Temperature [K]	
(1) H ₂ O, AlO, TiH, SiH, CH ₄ , CO, clouds, hazes, stellar activity	401.41		1539.70 ^{+317.21} _{-304.42}	
(2) H ₂ O, AlO, TiH, SiH, CH ₄ , CO, clouds, hazes	387.38	5.64 w.r.t. (1)	950.73 ^{+93.36} _{-83.04}	
(3) H ₂ O, clouds, stellar activity	401.68	< 1 w.r.t. (1)	1357.63 ^{+234.71} _{-263.14}	
(4) H ₂ O, AlO, TiH, SiH, clouds, hazes, stellar activity	401.14	< 1 w.r.t. (1)	1435.55 ^{+266.26} _{-282.96}	
(5) H ₂ O, TiO, VO, FeH, clouds, stellar activity	401.42	< 1 w.r.t. (1)	1550.71 ^{+306.26} _{-346.10}	

Case 3: WFC3				
Setup	Log Evidence	Sigma (discarded by)	Retrieved Temperature [K]	
(1) H ₂ O, AlO, TiH, SiH, CH ₄ , CO, clouds, hazes, stellar activity	285.37		1396.20 ^{+291.34} _{-243.79}	
(2) H ₂ O, AlO, TiH, SiH, CH ₄ , CO, clouds, hazes	278.77	4.05 w.r.t. (1)	900.56 ^{+153.18} _{-112.25}	
(3) H ₂ O, clouds, stellar activity	284.59	1.88 w.r.t. (1)	1374.81 ^{+378.09} _{-262.77}	
(4) H ₂ O, AlO, TiH, SiH, clouds, hazes, stellar activity	285.44	< 1 w.r.t. (1)	1356.01 ^{+256.60} _{-220.37}	
(5) H ₂ O, TiO, VO, FeH, clouds, stellar activity	284.15	2.15 w.r.t. (1)	1475.32 ^{+309.41} _{-311.57}	

spectral bin to counteract the flux loss. Our analysis returns a STIS data point at 0.87 μm that is at least 2σ away from the G102 datapoints placed between 0.8 and 0.94 μm . A similar decrease in transit depth at the same wavelengths was also recovered by [Sing et al. \(2016\)](#), as it can be seen in Figure 7. Yet, the transit depths of the white lightcurves for G750L and G102 are within 1σ of with each other (WFC3/G102: $R_p/R_* = 0.12184^{+0.00019}_{-0.00022}$; STIS/G750L: $R_p/R_* = 0.1211^{+0.0014}_{-0.0013}$), confirming that the two instrumental calibrations are in overall agreement. Finally, we must note that this problematic STIS/G750L datapoint is not statistically significant for the spectral modelling. From Figure 8 and 9 we can observe that the TauREx 3 atmospheric model ignores this data point when computing the best-fit spectrum.

On the other hand, between 3 and 5 μm lie the Spitzer data points, whose transit depths cannot be compared to any additional dataset. We shifted the two Spitzer data points 100 ppm up and 100 ppm down from their original position to check if the results would be con-

siderably impacted. In either case the retrieved mean molecular abundances and other atmospheric features such as radius and temperature, fluctuate at the order of the fifth decimal figure from the initial values, implying an accurate data reduction process and stability of the results.

An additional issue to take into account when combining datasets taken months or even years apart is atmospheric variability. We must remember that planets are dynamic bodies, varying in space and time. Hence, mechanisms like star-planet interaction and global circulation processes such as polar vortexes and zonal jets can produce very strong temperature and chemical differences ([Cho et al. 2003, 2021](#)). It might not be surprising that the same planet can display contrasting spectral features at the same wavelengths, such as the two opposite spectral trends we presented between ~ 0.4 and $\sim 0.6 \mu\text{m}$. In light of this, we must stress that the publicly available STIS observations used in this study, lack the post-egress part of the planetary transit (Figure 3, 4,

5). Missing lightcurve data strongly impacts the transit fit model, which then could potentially affect the derived transit depth, leading to discordant spectral features amongst different observations, as highlighted in Figure 7.

Due to the discrepancies in the data, we decided to model the contrasting STIS datasets separately: in Case 1 we considered a spectrum that includes STIS visit 1&3, WFC3, IRAC; in Case 2 we modelled the spectrum with STIS visit 2&3, WFC3, IRAC. Additionally, we employed the WFC3 observations alone (Case 3) to check how the results would change when we do not include the problematic STIS datasets.

To explain the unusually strong downward slope in the optical range displayed by the Case 2 spectrum (Figure 8, inset), an active star was included in the retrieval set-up. For consistency, we applied the same stellar model to Case 1 and Case 3 spectra. Potentially, STIS visit 2&3, being taken just a few days apart, were impacted by a stellar event, causing the spectrum to be best fitted by a model containing a high spots and faculae covering fraction. STIS visit 1 could have also been affected by a similar event, given that its best model favours stellar activity in place of aerosols.

Theoretically, a faculae covering fraction between 40 and 50% is unlikely in a F6-type star like WASP-17, unless we are dealing with a rare and extreme event. Moreover, we recognise that the posterior distributions between the faculae temperature and their covering fraction is degenerate (see Figure 8). This is because the retrieval is unable to distinguish between two scenarios: 1) a smaller covering fraction of hotter faculae and 2) a larger covering fraction of cooler faculae. Both scenarios result in similar stellar disk-integrated SEDs and thus introduce similar contamination features to the transmission spectrum.

There are no previous studies on the activity of the star so we are unable to compare our results with published research. However, Khalafinejad et al. (2018) mention that their attempt to identify a sodium feature in the spectrum of WASP-17 b could have been impacted by an in-transit activity of the host star, which decreased the planetary Na signal. Hence, stellar contamination cannot be excluded as an additional cause for a decreasing transit depth in the optical regime. Continuous photometric monitoring of WASP-17 is necessary to determine accurately the activity levels of the star.

When the star is treated as an homogeneous body, the retrieval of Case 1 spectrum results in a extremely high SiH volume mixing ratio $\log_{10}(\text{SiH}) = -3.85^{+1.18}_{-2.38}$. This result is unlikely, given that chemical equilibrium models predict a SiH abundance in the order of 10^{-16} at

900 K (Woitke et al. 2018). Perhaps, such high SiH abundance is due to a missing molecule which is not accounted for. Either this missing gas absorbs at the same wavelengths of SiH or it has similar absorption features. Even if we wanted to investigate this further, we do not possess all the possible molecular cross-sections and it is not feasible to test all the known molecules that absorb in the optical region. However, by inspecting the SiH results retrieved from the Case 2 and Case 3 spectra, we confirm that SiH is largely unconstrained and remains undetected.

Overall, we notice that when we consider an inactive star, the retrievals struggle to fit the data points at the end of the WFC3 wavelength coverage at ~ 1.6 - $1.8 \mu\text{m}$ and those at 0.4 - $0.55 \mu\text{m}$, especially visit 2 (see Figure 9, inset). This statement is supported by the log evidence of the models: when stellar activity is included, the $\log(E)$ increases by a minimum of 4σ (compared to the same model without stellar activity). Furthermore, independently of the datasets modelled, our results suggest the presence of the same trace gases (H₂O, AlO, TiH) as when accounting for a heterogeneous star. At this stage we do not possess enough evidence to discard a particular STIS dataset in favour of another one, but the information content derived by WFC3 data alone is enough to propose the existence of those species in the atmosphere of WASP-17 b.

No previous study has detected any metal hydrates or oxides in the atmosphere of this particular hot-Jupiter, albeit Bento et al. (2014) searching for TiO signatures in the upper atmosphere of WASP-17b. Theoretical studies by Fortney et al. (2008) propose the presence of TiO and VO in the atmosphere of planets with large day-night temperature contrasts. We do not exclude the presence of these trace gases but our analyses favour a model containing AlO, TiH, SiH, CH₄ and CO rather than TiO, VO and FeH by a 2.6σ evidence, when applied to the spectrum in Case 1 (Table 3). As of yet, this is the first time that the presence of AlO and TiH has been suggested in the atmosphere of WASP-17 b.

During our preliminary retrievals, we tested different models containing a variety of trace gases on the spectrum in Case 1, but ultimately we found that including H₂O, AlO, TiH, SiH, clouds, hazes and an active star would lead to the best results. Adding CH₄ and CO in the latter model did not substantially affect the Bayesian evidence, the two models being 0.26σ away from each other.

On the other hand, the spectrum containing STIS visit 2 proved trickier to model. Out of the five models tested on these data, model (1), (3), (4) and (5) in Table 3 (middle panel) were within less than 1σ of each other,

and model (2) containing H_2O , AlO , TiH , SiH , CH_4 , CO clouds and hazes was 5.64σ away from model (1), which includes the same chemical species plus stellar variability. Ultimately, we used the best-fit model for the Case 1 spectral scenario also in the Case 2 dataset and on the WFC3 data alone, to make a valid comparison between the scenarios in terms of molecular abundances. The retrievals conducted exclusively on the WFC3 data too favour a model containing H_2O , AlO , TiH , SiH , clouds, hazes, stellar spots and faculae.

Our results suggest that WASP-17b possesses mostly a clear atmosphere, free from a thick layer of clouds and aerosols. [Sing et al. \(2016\)](#) report the atmosphere of this hot-Jupiter to be the clearest among the 10 exoplanets in their study, presenting distinct water features. [Pinhas et al. \(2018\)](#) find similar results, their spectrum being fitted best by a model containing mostly a cloudless atmosphere with a cloud/haze fraction of 0.2 and a cloud top pressure of 0.1 mbar. On the other hand, [Barstow et al. \(2016\)](#) report the presence of scattering aerosols at relatively high altitudes, but not so strong to reduce the size of the other molecular features. [Mandell et al. \(2013\)](#) also claim that their data is best fitted by a model that accounts for hazes or clouds.

We were unable to identify the alkali lines (Na , K) reported by [Sing et al. \(2016\)](#). Their data point at $\sim 0.6\text{ }\mu\text{m}$ has an uncertainty three times larger than the other ones and it is not statistically significant to demonstrate the presence of sodium in the atmosphere of WASP-17b.

Furthermore, during our exploratory retrievals we did not find evidence of CO_2 which, on the contrary, is detected by [Alderson et al. \(2022\)](#). Due to the sparse nature of the Spitzer datapoints and the influence that additional molecules can impart in the spectrum of an exoplanet at the wavelengths probed by IRAC, it is challenging to place precise constraints on the abundance of carbon-bearing molecules.

Regardless of whether we consider an active star or not, the retrieved planetary temperature is always lower than the calculated equilibrium temperature, as transmission studies often find. Discrepancies between the retrieved and the calculated temperatures have been analysed by several authors, e.g. [Caldas et al. \(2019\)](#); [MacDonald et al. \(2020\)](#); [Pluriel et al. \(2020a\)](#); [Changeat et al. \(2021\)](#), and found to arise from a combination of aspects: the adoption of 1D atmospheric models to describe the different molecular content of the morning and evening terminators, the use of simplified models to characterise the planets' 3D processes and the adoption of incorrect assumptions regarding the albedo and the emissivity when calculating the planet's equilibrium

temperature. Hence, retrieving a lower temperature than calculated should not be surprising.

5. CONCLUSION

Remote-sensing studies are the only technique through which we can unveil the atmospheric characteristics of planets outside our solar system. In recent years the *Hubble Space Telescope* has pioneered the spectroscopic investigation of exoplanets. In this study we presented the transmission spectrum of WASP-17b observed with the Space Telescope Imaging Spectrograph and the Wide Field Camera 3 mounted on HST, and the Infrared Camera Array aboard the Spitzer Space Telescope. The Hubble spectroscopic data was reduced with Iraclis, a specialised STIS and WFC3 data reduction routine. Photometric data obtained by Spitzer was instead reduced and analysed with the TLCD-LSTM method by means of a long short-term memory network. Given the discordant results obtained for two STIS observations which cover the same wavelength range, we decided to model the spectrum of WASP-17b in three separate cases: (a) including STIS visit 1&3, WFC3, IRAC (Case 1); (b) including STIS visit 2&3, WFC3, IRAC (Case 2); (c) WFC3 only (Case 3). The fully Bayesian retrieval framework TauREx 3 was then employed to find the model that can best explain each spectral scenario. Retrieval results find that the best-fit model is constituted by H_2O , AlO , TiH , SiH , clouds, hazes and stellar activity in Case 1 and 3. The best-fit model for Case 2 includes CH_4 and CO too, however their addition only improved the Bayesian evidence by 0.26σ . We acknowledge that the extreme stellar activity identified on the F6-type host star is unlikely, therefore we check if a model containing the same trace gases but including an homogeneous star is able to describe all three spectra. Independently of the activity of the star, our analysis indicates the presence of water in the solar/super-solar regime and possible traces of AlO and TiH in the atmosphere of WASP-17b. The atmosphere of the inflated hot-Jupiter appears to be free from both an optically thick layer of gray clouds and hazes. Given the incompleteness of the STIS lightcurves, we reckon that additional HST/STIS observations will help to improve our knowledge about the limb of this gas giant. In fact, the remarkable large scale height of WASP-17b, makes the planet a perfect target for further atmospheric characterisation, both from the ground and by current and next generation space-based observatories such as JWST ([Greene et al. 2016](#)) and Ariel ([Tinetti et al. 2018](#)).

ACKNOWLEDGEMENTS

We thank our anonymous referee for the insightful comments which have improved the quality of our work.

Data: This work is based upon observations with the NASA/ESA Hubble Space Telescope, obtained at the Space Telescope Science Institute (STScI) operated by AURA, Inc. The publicly available HST observations presented here were taken as part of proposal 12473 and 14918, led by David Sing and Hannah Wakeford respectively. These were obtained from the Hubble Archive which is part of the Mikulski Archive for Space Telescopes. This work is also based in part on observations made with the Spitzer Space Telescope, which is operated by the Jet Propulsion Laboratory, California Institute of Technology, under a contract with NASA. The publicly available Spitzer data were taken as part of programme 90092 led by Jean-Michel Desert. This paper also uses data collected by the TESS mission, which are publicly available from the Mikulski Archive for Space Telescopes (MAST) and produced by the Science Processing Operations Center (SPOC) at NASA Ames Research Center (Jenkins et al. 2016). Funding for the TESS mission is provided by NASA's Science Mission Directorate. We are thankful to those who operate this archive, the public nature of which increases scientific productivity and accessibility (Peek et al. 2019).

Funding: This project has received funding from the European Research Council under the European Union's Horizon 2020 research and innovation program (grant agreement No. 758892, ExoAI) and the European Union's Horizon 2020 COMPET program (grant agreement No. 776403, ExoPLANETS A). Furthermore, we acknowledge funding by the UK Space Agency and Science and Technology Funding Council grants ST/K502406/1, ST/P000282/1, ST/P002153/1, ST/S002634/1, ST/T001836/1, ST/V003380/1 and ST/W00254X/1. BE is a Laureate of the Paris Region fellowship programme which is supported by the Ile-de-France Region and has received funding under the Horizon 2020 innovation framework programme and the Marie Skłodowska-Curie grant agreement no. 945298.

Software: Iraclis (Tsiaras et al. 2016b), TauREx3 (Al-Refaie et al. 2021), PyLightcurve (Tsiaras et al. 2016a), Lightkurve (Cardoso et al. 2018), ExoTETHyS (Morello et al. 2020), Astropy (Price-Whelan et al. 2018), h5py (Collette 2013), emcee (Foreman-Mackey et al. 2013), Matplotlib (Hunter 2007), Multinest (Feroz et al. 2009a), PyMultinest (Buchner et al. 2014), Pandas (McKinney et al. 2011), Numpy (Oliphant 2006), SciPy (Virtanen et al. 2020), corner (Foreman-Mackey 2016).

REFERENCES

Abel, M., Frommhold, L., Li, X., & Hunt, K. L. C. 2011, *The journal of physical chemistry. A*, 115, 6805–6812. <https://doi.org/10.1021/jp109441f>

—. 2012, *The Journal of chemical physics*, 136, 044319. <https://doi.org/10.1063/1.3676405>

Al-Refaie, A. F., Changeat, Q., Waldmann, I. P., & Tinetti, G. 2021, *The Astrophysical Journal*, 917, 37. <http://dx.doi.org/10.3847/1538-4357/ac0252>

Alderson, L., Wakeford, H., MacDonald, R., et al. 2022, *Monthly Notices of the Royal Astronomical Society*, 512, 4185

Allard, F., Homeier, D., Freytag, B., Schaffenberger, W., & Rajpurohit, A. 2013, arXiv preprint arXiv:1302.6559

Allard, N., Spiegelman, F., Leininger, T., & Molliere, P. 2019, *Astronomy & Astrophysics*, 628, A120

Anderson, D., Smith, A., Lanotte, A., et al. 2011, *Monthly Notices of the Royal Astronomical Society*, 416, 2108

Anderson, D. R., Hellier, C., Gillon, M., et al. 2010, *ApJ*, 709, 159

Anisman, L. O., Edwards, B., Changeat, Q., et al. 2020, *The Astronomical Journal*, 160, 233

Arcangeli, J., Désert, J.-M., Parmentier, V., et al. 2019, *Astronomy & Astrophysics*, 625, A136

Barstow, J. K., Aigrain, S., Irwin, P. G., & Sing, D. K. 2016, *The Astrophysical Journal*, 834, 50

Bate, M., Lodato, G., & Pringle, J. 2010, *Monthly Notices of the Royal Astronomical Society*, 401, 1505

Bayliss, D. D. R., Winn, J. N., Mardling, R. A., & Sackett, P. D. 2010, *ApJL*, 722, L224

Bento, J., Wheatley, P., Copperwheat, C., et al. 2014, *Monthly Notices of the Royal Astronomical Society*, 437, 1511

Bostroem, K., & Proffitt, C. 2011, *STIS Data Handbook*

Bourrier, V., Lovis, C., Beust, H., et al. 2018, *Nature*, 553, 477

Buchner, J., Georgakakis, A., Nandra, K., et al. 2014, *Astronomy & Astrophysics*, 564, A125

Caldas, A., Leconte, J., Selsis, F., et al. 2019, *Astronomy & Astrophysics*, 623, A161

Cardoso, J. V. d. M., Hedges, C., Gully-Santiago, M., et al. 2018, *Astrophysics Source Code Library*, ascl

Carone, L., Mollière, P., Zhou, Y., et al. 2021, *Astronomy & Astrophysics*, 646, A168

Changeat, Q., Al-Refaie, A. F., Edwards, B., Waldmann, I. P., & Tinetti, G. 2021, *The Astrophysical Journal*, 913, 73

Changeat, Q., Edwards, B., Al-Refaie, A. F., et al. 2020, *The Astronomical Journal*, 160, 260

Charnay, B., Blain, D., Bézard, B., et al. 2021, *Astronomy & Astrophysics*, 646, A171

Cho, J. Y., Menou, K., Hansen, B. M., & Seager, S. 2003, *The Astrophysical Journal Letters*, 587, L117

Cho, J. Y., Skinner, J. W., & Thrastarson, H. T. 2021, *The Astrophysical Journal Letters*, 913, L32

Chubb, K. L., Rocchetto, M., Yurchenko, S. N., et al. 2021, *Astronomy & Astrophysics*, 646, A21

Ciardi, D. R., Von Braun, K., Bryden, G., et al. 2011, *The Astronomical Journal*, 141, 108

Claret, A. 2000, *A&A*, 363, 1081

Coles, P. A., Yurchenko, S. N., & Tennyson, J. 2019, *Monthly Notices of the Royal Astronomical Society*, 490, 4638

Collette, A. 2013, *Python and HDF5: unlocking scientific data* (" O'Reilly Media, Inc.")

Dulick, M., Bauschlicher Jr, C., Burrows, A., et al. 2003, *The Astrophysical Journal*, 594, 651

Edwards, B., Changeat, Q., Baeyens, R., et al. 2020a, *The Astronomical Journal*, 160, 8

Edwards, B., Changeat, Q., Mori, M., et al. 2020b, *The Astronomical Journal*, 161, 44

Feng, Y. K., Line, M. R., & Fortney, J. J. 2020, *The Astronomical Journal*, 160, 137

Feroz, F., Hobson, M., & Bridges, M. 2009a, *Monthly Notices of the Royal Astronomical Society*, 398, 1601

Feroz, F., Hobson, M. P., & Bridges, M. 2009b, *Monthly Notices of the Royal Astronomical Society*, 398, 1601. <https://doi.org/10.1111/j.1365-2966.2009.14548.x>

Fletcher, L. N., Gustafsson, M., & Orton, G. S. 2018, *The Astrophysical Journal Supplement Series*, 235, 24. <http://dx.doi.org/10.3847/1538-4365/aaa07a>

Fleury, B., Gudipati, M. S., Henderson, B. L., & Swain, M. 2019, *The Astrophysical Journal*, 871, 158

Foreman-Mackey, D. 2016, *The Journal of Open Source Software*, 1, 24

Foreman-Mackey, D., Hogg, D. W., Lang, D., & Goodman, J. 2013, *Publications of the Astronomical Society of the Pacific*, 125, 306

Fortney, J. J., Lodders, K., Marley, M. S., & Freedman, R. S. 2008, *The Astrophysical Journal*, 678, 1419

Gharib-Nezhad, E., Iyer, A. R., Line, M. R., et al. 2021, *The Astrophysical Journal Supplement Series*, 254, 34

Gordon, I., Rothman, L. S., Wilzewski, J. S., et al. 2016, in *AAS/Division for Planetary Sciences Meeting Abstracts*, Vol. 48, *AAS/Division for Planetary Sciences Meeting Abstracts* #48, 421.13

Goyal, J. M., Mayne, N., Drummond, B., et al. 2020, *Monthly Notices of the Royal Astronomical Society*, 498, 4680

Greene, T. P., Line, M. R., Montero, C., et al. 2016, *The Astrophysical Journal*, 817, 17

Guilluy, G., Gressier, A., Wright, S., et al. 2020, *The Astronomical Journal*, 161, 19

Guo, X., Crossfield, I. J., Dragomir, D., et al. 2020, *The Astronomical Journal*, 159, 239

Hébrard, G., Ehrenreich, D., Bouchy, F., et al. 2011, *Astronomy & Astrophysics*, 527, L11

Hochreiter, S., & Schmidhuber, J. 1997, *Neural computation*, 9, 1735

Hunter, J. D. 2007, *Computing in science & engineering*, 9, 90

Husser, T.-O., Wende-von Berg, S., Dreizler, S., et al. 2013, *Astronomy & Astrophysics*, 553, A6

Ida, S., & Lin, D. 2004, *The Astrophysical Journal*, 616, 567

Irwin, P. G., Parmentier, V., Taylor, J., et al. 2020, *Monthly Notices of the Royal Astronomical Society*, 493, 106

Jenkins, J. M., Twicken, J. D., McCauliff, S., et al. 2016, in *Software and Cyberinfrastructure for Astronomy IV*, Vol. 9913, International Society for Optics and Photonics, 99133E

Johnson, J. A., Winn, J. N., Albrecht, S., et al. 2009, *Publications of the Astronomical Society of the Pacific*, 121, 1104

Kawashima, Y., & Ikoma, M. 2018, *The Astrophysical Journal*, 853, 7

Khalafinejad, S., Salz, M., Cubillos, P. E., et al. 2018, *A&A*, 618, A98

Knutson, H. A., Lewis, N., Fortney, J. J., et al. 2012, *The Astrophysical Journal*, 754, 22

Kokori, A., Tsiaras, A., Edwards, B., et al. 2021, *Experimental Astronomy*, doi:10.1007/s10686-020-09696-3. <http://dx.doi.org/10.1007/s10686-020-09696-3>

Kramida, A. 2013, *Fusion Science and Technology*, 63, 313

Kreidberg, L., Line, M. R., Parmentier, V., et al. 2018, *The Astronomical Journal*, 156, 17

Lee, J.-M., Heng, K., & Irwin, P. G. 2013, *The Astrophysical Journal*, 778, 97

Li, G., Gordon, I. E., Rothman, L. S., et al. 2015, *The Astrophysical Journal Supplement Series*, 216, 15. <https://doi.org/10.1088/0067-0049/216/1/15>

Lin, D. N., Bodenheimer, P., & Richardson, D. C. 1996, *Nature*, 380, 606

MacDonald, R. J., Goyal, J. M., & Lewis, N. K. 2020, *ApJL*, 893, L43

Mamajek, E. E., & Hillenbrand, L. A. 2008, *The Astrophysical Journal*, 687, 1264

Mandell, A. M., Haynes, K., Sinukoff, E., et al. 2013, *The Astrophysical Journal*, 779, 128

McKemmish, L. K., Masseron, T., Hoeijmakers, H. J., et al. 2019, *Monthly Notices of the Royal Astronomical Society*, 488, 2836

McKemmish, L. K., Yurchenko, S. N., & Tennyson, J. 2016, *Monthly Notices of the Royal Astronomical Society*, 463, 771

McKinney, W., et al. 2011, *Python for high performance and scientific computing*, 14, 1

McQuillan, A., Mazeh, T., & Aigrain, S. 2014, *The Astrophysical Journal Supplement Series*, 211, 24

Mikal-Evans, T., Sing, D. K., Goyal, J. M., et al. 2019, *Monthly Notices of the Royal Astronomical Society*, 488, 2222

Morello, G., Claret, A., Martin-Lagarde, M., et al. 2020, *The Astronomical Journal*, 159, 75

Morvan, M., Nikolaou, N., Tsiaras, A., & Waldmann, I. P. 2020, *The Astronomical Journal*, 159, 109

Mugnai, L. V., Modirrousta-Galian, D., Edwards, B., et al. 2021, *The Astronomical Journal*, 161, 284

Nagasawa, M., Ida, S., & Bessho, T. 2008, *The Astrophysical Journal*, 678, 498

Norris, C. M., Beeck, B., Unruh, Y. C., et al. 2017, *Astronomy & Astrophysics*, 605, A45

Oliphant, T. E. 2006, *A guide to NumPy*, Vol. 1 (Trelgol Publishing USA)

Patrascu, A. T., Yurchenko, S. N., & Tennyson, J. 2015, *Monthly Notices of the Royal Astronomical Society*, 449, 3613

Peek, J. E., Desai, V., White, R. L., et al. 2019, arXiv preprint arXiv:1907.06234

Pinhas, A., Madhusudhan, N., Gandhi, S., & MacDonald, R. 2018, *Monthly Notices of the Royal Astronomical Society*, 482, 1485. <https://doi.org/10.1093/mnras/sty2544>

Pluriel, W., Zingales, T., Leconte, J., & Parmentier, V. 2020a, arXiv preprint arXiv:2003.05943

Pluriel, W., Whiteford, N., Edwards, B., et al. 2020b, *The Astronomical Journal*, 160, 112

Polyansky, O. L., Kyuberis, A. A., Zobov, N. F., et al. 2018, *Monthly Notices of the Royal Astronomical Society*, 480, 2597. <https://doi.org/10.1093/mnras/sty1877>

Price-Whelan, A. M., Sipócz, B., Günther, H., et al. 2018, *The Astronomical Journal*, 156, 123

Prichard, L., Welty, D., & Jones, A. 2022, *STIS Instrument Handbook for Cycle 30 v. 21*, 21, 21

Rackham, B., Espinoza, N., Apai, D., et al. 2017, *The Astrophysical Journal*, 834, 151

Rackham, B. V., Apai, D., & Giampapa, M. S. 2018, *The Astrophysical Journal*, 853, 122

—. 2019, *The Astronomical Journal*, 157, 96

Ricker, G. R., Winn, J. N., Vanderspek, R., et al. 2014, *Journal of Astronomical Telescopes, Instruments, and Systems*, 1, 014003

Robinson, T. D., & Catling, D. C. 2014, *Nature Geoscience*, 7, 12

Rothman, L. S., & Gordon, I. E. 2014, in 13th International HITRAN Conference, 49

Rothman, L. S., Gamache, R. R., Goldman, A., et al. 1987, *Applied optics*, 26, 4058

Rothman, L. S., Gordon, I. E., Barber, R. J., et al. 2010, *JQSRT*, 111, 2139

Rothman, L. S., Gordon, I., Barber, R., et al. 2010, *Journal of Quantitative Spectroscopy and Radiative Transfer*, 111, 2139

Sedaghati, E., Boffin, H. M. J., Jeřabková, T., et al. 2016, *A&A*, 596, A47

Sharp, C. M., & Burrows, A. 2007, *The Astrophysical Journal Supplement Series*, 168, 140

Shulyak, D., Lara, L. M., Rengel, M., & Némec, N.-E. 2020, *Astronomy & Astrophysics*, 639, A48

Simpson, E., Pollacco, D., Cameron, A. C., et al. 2011, *Monthly Notices of the Royal Astronomical Society*, 414, 3023

Sing, D. K., Fortney, J. J., Nikolov, N., et al. 2016, *Nature*, 529, 59

Skaf, N., Bieger, M. F., Edwards, B., et al. 2020, *The Astronomical Journal*, 160, 109

Southworth, J., Hinse, T. C., Dominik, M., et al. 2012, *MNRAS*, 426, 1338

Stevenson, K. B., Line, M. R., Bean, J. L., et al. 2017, *The Astronomical Journal*, 153, 68

Tennyson, J., Yurchenko, S. N., Al-Refaie, A. F., et al. 2016, *Journal of Molecular Spectroscopy*, 327, 73

Tinetti, G., Drossart, P., Eccleston, P., et al. 2018, *Experimental Astronomy*, 46, 135

Triaud, A. H., Cameron, A. C., Queloz, D., et al. 2010, *Astronomy & Astrophysics*, 524, A25

Tsiaras, A., Waldmann, I., Rocchetto, M., et al. 2016a, *The Astrophysical Journal*, 832, 202

Tsiaras, A., Waldmann, I. P., Tinetti, G., Tennyson, J., & Yurchenko, S. N. 2019, *Nature Astronomy*, 3, 1086

Tsiaras, A., Rocchetto, M., Waldmann, I., et al. 2016b, *The Astrophysical Journal*, 820, 99

Tsiaras, A., Waldmann, I., Zingales, T., et al. 2018, *The Astronomical Journal*, 155, 156

Venot, O., & Agúndez, M. 2015, *Experimental Astronomy*, 40, 469

Venot, O., Hébrard, E., Agúndez, M., Decin, L., & Bounaceur, R. 2015, *Astronomy & Astrophysics*, 577, A33

Venot, O., Hébrard, E., Agúndez, M., et al. 2012, *Astronomy & Astrophysics*, 546, A43

Virtanen, P., Gommers, R., Oliphant, T. E., et al. 2020, *Nature methods*, 17, 261

Wende, S., Reiners, A., Seifahrt, A., & Bernath, P. 2010, *Astronomy & Astrophysics*, 523, A58

Winn, J. N., Johnson, J. A., Fabrycky, D., et al. 2009, *The Astrophysical Journal*, 700, 302

Woitke, P., Helling, C., Hunter, G., et al. 2018, *Astronomy & Astrophysics*, 614, A1

Wood, P. L., Maxted, P. F. L., Smalley, B., & Iro, N. 2011, *MNRAS*, 412, 2376

Yip, K. H., Changeat, Q., Edwards, B., et al. 2020, *The Astronomical Journal*, 161, 4

Yurchenko, S. N., Sinden, F., Lodi, L., et al. 2018, *Monthly Notices of the Royal Astronomical Society*, 473, 5324

Yurchenko, S. N., & Tennyson, J. 2014, *Monthly Notices of the Royal Astronomical Society*, 440, 1649–1661. <http://dx.doi.org/10.1093/mnras/stu326>

Zhou, G., & Bayliss, D. D. R. 2012, *MNRAS*, 426, 2483

APPENDIX

A. NETWORK PARAMETERS USED FOR DETRENDING IRAC OBSERVATIONS

Table 4. Table of parameters used for detrending IRAC observations of WASP-17 b.

	Irac Channel 1	Irac Channel 2
Program	90092	90092
Aorkey	47040000	47039488
Radius [pixels]	3.25	3.25
Centroiding method	2D Gaussian	2D Gaussian
Start of test set [BMJD TDB]	56422.595	56426.330
End of test set [BMJD TDB]	56422.783	56426.518
# layers	2	2
# units	512	512
Dropout rate	10%	10%
Adam learning rate	0.005	0.005
β decay rate	0.95	0.95

B. SPECTRAL DATA

Table 5. Reduced and fitted spectral data from the raw HST/STIS transmission data using Iraclis.

Wavelength [μm]	Transit depth [%]	Error [%]	Bandwidth [μm]	Instrument	Grating
0.385	1.593	0.045	0.050	HST STIS	G430L
0.420	1.529	0.030	0.020	HST STIS	G430L
0.440	1.525	0.037	0.020	HST STIS	G430L
0.460	1.537	0.028	0.020	HST STIS	G430L
0.480	1.484	0.027	0.020	HST STIS	G430L
0.500	1.473	0.029	0.020	HST STIS	G430L
0.520	1.525	0.027	0.020	HST STIS	G430L
0.540	1.534	0.036	0.020	HST STIS	G430L
0.560	1.472	0.041	0.020	HST STIS	G430L
0.385	1.391	0.032	0.050	HST STIS	G430L
0.420	1.444	0.046	0.020	HST STIS	G430L
0.440	1.417	0.028	0.020	HST STIS	G430L
0.460	1.407	0.026	0.020	HST STIS	G430L
0.480	1.400	0.027	0.020	HST STIS	G430L
0.500	1.431	0.026	0.020	HST STIS	G430L
0.520	1.444	0.027	0.020	HST STIS	G430L
0.540	1.466	0.033	0.020	HST STIS	G430L
0.560	1.486	0.037	0.020	HST STIS	G430L
0.570	1.479	0.021	0.040	HST STIS	G750L
0.605	1.456	0.036	0.030	HST STIS	G750L
0.635	1.464	0.034	0.030	HST STIS	G750L
0.665	1.440	0.027	0.030	HST STIS	G750L
0.700	1.488	0.022	0.040	HST STIS	G750L
0.760	1.497	0.033	0.080	HST STIS	G750L
0.870	1.394	0.031	0.140	HST STIS	G750L

Table 6. Reduced and fitted spectral data from the raw Spitzer/IRAC transmission data using TLCD-LSTM.

Wavelength [μm]	Transit depth [%]	Error [%]	Bandwidth [μm]	Instrument
3.560	1.500	0.032	0.380	Spitzer IRAC
4.500	1.521	0.018	0.560	Spitzer IRAC

Table 7. Reduced and fitted spectral data from the raw HST/WFC3 transmission data using Iraclis.

Wavelength [μm]	Transit depth [%]	Error [%]	Bandwidth [μm]	Instrument	Grism
0.813	1.506	0.019	0.025	HST WFC3	G102
0.838	1.492	0.012	0.025	HST WFC3	G102
0.863	1.483	0.009	0.025	HST WFC3	G102
0.888	1.479	0.011	0.025	HST WFC3	G102
0.913	1.459	0.007	0.025	HST WFC3	G102
0.938	1.504	0.009	0.025	HST WFC3	G102
0.963	1.502	0.010	0.025	HST WFC3	G102
0.988	1.497	0.012	0.025	HST WFC3	G102
1.013	1.484	0.009	0.025	HST WFC3	G102
1.038	1.474	0.009	0.025	HST WFC3	G102
1.063	1.474	0.008	0.025	HST WFC3	G102
1.088	1.480	0.010	0.025	HST WFC3	G102
1.113	1.493	0.009	0.025	HST WFC3	G102
1.138	1.471	0.020	0.025	HST WFC3	G102
1.126	1.519	0.011	0.022	HST WFC3	G141
1.148	1.507	0.012	0.021	HST WFC3	G141
1.169	1.491	0.011	0.021	HST WFC3	G141
1.189	1.488	0.009	0.020	HST WFC3	G141
1.208	1.489	0.011	0.019	HST WFC3	G141
1.228	1.500	0.008	0.019	HST WFC3	G141
1.246	1.476	0.009	0.019	HST WFC3	G141
1.266	1.469	0.011	0.019	HST WFC3	G141
1.285	1.457	0.013	0.019	HST WFC3	G141
1.304	1.503	0.010	0.019	HST WFC3	G141
1.323	1.497	0.009	0.019	HST WFC3	G141
1.341	1.514	0.010	0.019	HST WFC3	G141
1.361	1.537	0.014	0.019	HST WFC3	G141
1.380	1.522	0.012	0.020	HST WFC3	G141
1.400	1.516	0.011	0.020	HST WFC3	G141
1.420	1.517	0.011	0.020	HST WFC3	G141
1.441	1.518	0.011	0.021	HST WFC3	G141
1.462	1.527	0.012	0.021	HST WFC3	G141
1.483	1.526	0.009	0.022	HST WFC3	G141
1.505	1.493	0.011	0.022	HST WFC3	G141
1.528	1.500	0.009	0.023	HST WFC3	G141
1.552	1.488	0.011	0.024	HST WFC3	G141
1.576	1.463	0.010	0.025	HST WFC3	G141
1.602	1.459	0.011	0.026	HST WFC3	G141
1.629	1.436	0.010	0.028	HST WFC3	G141

C. RETRIEVAL CONTRIBUTION FUNCTIONS

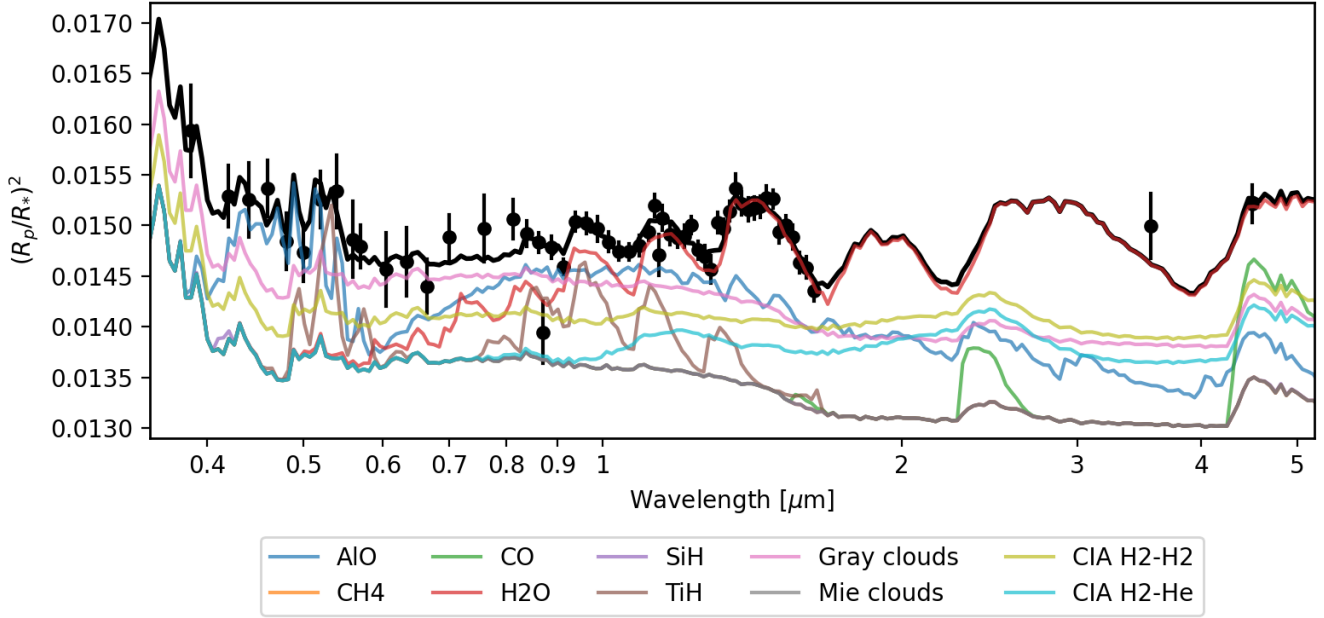


Figure 10. STIS visit 1&3, WFC3 and Spitzer data (Case 1) fitted by the best-fit model (black line) that includes an active star together with the contributions from CIA, active trace gases, clouds and hazes. Stellar activity induces wavelength variations at the base of the model, reason why the gray clouds and Mie clouds contributions are not flat at the bottom.

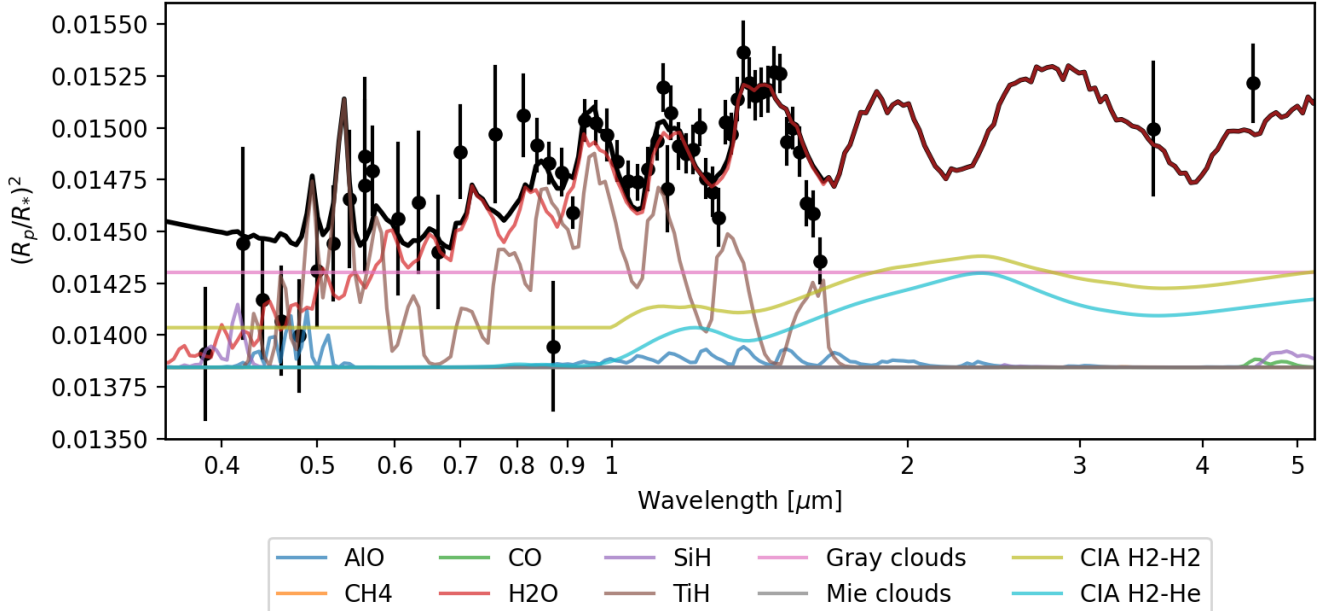


Figure 11. STIS visit 2&3, WFC3 and Spitzer data (Case 2) fitted by the best-fit model (black line) that includes a homogeneous star together with the contributions from CIA, active trace gases, clouds and hazes.